Soil Dynamics and Earthquake Engineering 123 (2019) 144–161

Contents lists available at ScienceDirect

Soil Dynamics and Earthquake Engineering

journal homepage: www.elsevier.com/locate/soildyn

Simulation of spatially variable seismic underground motions in saturated double-phase media with overlying water excited by SV-wave and difference from P-wave incidence

Guohuan Liu[a,b,*], Yaqiang Liu[b], Xiao Feng[b], Dongsheng Wang[c]

[a] State Key Laboratory of Hydraulic Engineering Simulation and Safety, Tianjin University, Tianjin, China
[b] School of Civil Engineering, Tianjin University, Tianjin, China
[c] School of Civil and Transportation Engineering, Hebei University of Technology, Tianjin, China

ARTICLE INFO

Keywords:
Double-phase media
Overlying water
Multi-support seismic underground excitations
Underground power spectral density
Underground response spectrum
Underground coherency function

ABSTRACT

The spatial seismic excitations affected by water-saturated soil, a double-phase medium, and overlying water are desirable to be considered for evaluating the seismic response of some typical structures such as large-span cross-sea bridges considering soil-structure interaction. This paper focuses on the study of a theoretical method and numerical simulation of multi-support seismic underground excitations in saturated soil with overlying water for obliquely incident *SV* waves that can produce *P*1, *P*2 and *SV* waves in saturated soil. First, the reflection coefficients (results are different from the case for P waves incidence) of three kinds of waves (*P*1, *P*2, *SV*) at the interface between saturated soil and overlying water are derived. Based on the reflection coefficients and the boundary conditions at the elastic solid-saturated soil interface, the transfer functions of soil layers with arbitrary depths are proposed to calculate the key elements (i.e., the underground power spectral density, response spectrum function and underground coherency function) for generating the multi-support seismic underground motions. Second, these three key elements are used to establish the underground power spectral matrix, and then the underground motions are generated by decomposing the matrix. Finally, the method is verified by numerical examples and the influences of overlying water depth and incident angle on ground motions are investigated. The effect of incident angle on transfer functions show great difference between the small-angle and large-angle case. Moreover, the phenomenon that is diffrent from P-waves incidence case is investigated,found and emphasized, and the reasons are given.

1. Introduction

In practical cross-sea engineering, the soil below the see bed is filled with water. Therefore, the related research considering water-saturated soil (especially the saturated soil that affected by overlying water) on ground motions is desirable for the evaluation of the seismic response of cross-sea structures. Biot [1–3] established the propagation theory of porous elastic waves that laid the foundation for the study of wave propagations in saturated medium. Deresiewicz [4–7] systematically studied the propagation characteristics of waves at the interface of saturated soil. In addition, the relevant studies on transmission and reflection of waves at different interfaces have also been carried out by many researchers. Considering the loss effect of the media on seismic energy, Mott [8] studied the reflection and transmission of waves at the fluid-solid interface. Brekhovskikh [9] introduced the theory of transmission and reflection of waves at the interface of elastic solid-ideal fluid. Dorman [10] gave a simple expression for period equation for surface waves of the Rayleigh type on half space of solid and liquid layers arbitrarily interspersed. The simple expression provides a convenient approach for computing the surface wave dispersion. Considering the energy dissipation, Zhao et al. [11] deduced the formula for the refraction and reflection coefficients at the interface between solid and fluid-saturated porous media based on the continuous conditions. In addition, the effects of seawater layer on ground motions have also been studied. Petukhin et al. studied the effect of the oceanic water layer on strong ground motions and the results showed that the water layer has a significant effect on the fundamental mode of the shallow Rayleigh wave. In contrast, the effect of the water layer on deep earthquakes can be neglected for ground motions at land sites [12]. Maeda et al. [13] conducted a large-scale, parallel computer simulation using the finite-difference method (FDM) with newly developed tsunami-coupled equations of motion to systematically understand the

* Corresponding author.
E-mail address: liugh@tju.edu.cn (G. Liu).

https://doi.org/10.1016/j.soildyn.2019.04.009
Received 31 March 2018; Received in revised form 28 December 2018; Accepted 8 April 2019

hazards including strong ground motions, coseismic ground deformation, and tsunamis in the 2011 Tohoku earthquake. Pitarka [14] studied the effects of seawater layer and ocean-bottom topography on the sea floor seismic waveforms and teleseismic distances from offshore earthquakes by simulating ground motions from shallow double-couple point sources using a 3D subduction zone seismic velocity model. Diao et al. [15] studied the effect of seawater on vertical ground motions via a theoretical method and then analyzed actual offshore ground motion records using a statistical method. Todoriki et al. [16] investigated the effect of sea water on the propagation of seismic waves using a 3D finite-difference-method simulation of seismic wave propagation following offshore earthquakes. The significance of the seawater layer to model offshore earthquakes was demonstrated.

On the other hand, the earthquake ground motions spatial variability (e.g., the travelling wave effect, site coherent effect and local site effect) can significantly influence the response of long-span cross-sea structures [17–26]. Therefore, it is not sufficient to only consider the effects of saturated soil and overlying water on ground motions for these structures. Numerical method has its disadvantage of investigating relative complex site or terrain (especially for those saturated soil with overlying water). The required fine discretization of the computational domain has definitely and significantly resulted in its computation non-convergence.. This essentially limits the applications of the numerical methods for engineering practice and requires an approach (such as the analytical solution derived from wave propagation theories) by which the required convergent and accurate analysis results can be definitely obtained. Besides, the analytical methods are essential for exploring the physical nature of particular problem and can be referred for the accuracy verification of the different numerical method. Hao et al. [27] used the spectral representation method to simulate spatially varying ground motions based on the assumption that all spatially varying ground motions have the same intensity. And a high efficient scheme was proposed to achieve simulation efficiency for conditions that the number of locations is large [28]. This method was extended by Bi and Hao [29,30] to simulate spatially varying ground motions at sites under varying conditions. By investigating the influences of layered irregular sites and random soil properties on coherency functions, an approximate method was presented to simulate the spatially varying ground motions on the surface of the non-uniform sites at different locations. Furthermore, this method was extended to conditionally simulate spatially varying ground motions [31] and simulate non-stationary non-Gaussian spatially varying ground motions [32].

Deodatis [33] presented a method to simulate spatial ground motions with different power spectral densities at different locations and studied the influence of spatial variation of earthquake ground motion on the seismic response of large embankment dams. Afterwards, considering the wave propagation and loss of coherence effects, Deodatis et al. [34]studied the influence of spatial variation ground motions on the SR14/I-5 interchange and three-span concrete bridge. To generate the ground motion time histories taking into account both time factor and spatial variability, Cacciola et al. [35] proposed a spectral-representation-based method for generating fully non-stationary and spectrum-compatible ground motion vector processes at different locations on the ground surface. The method can be used for reliability studies in an analytic stochastic fashion. Zentner and Poirion [36] introduced a new method for generating synthetic ground motions based on Karhunen-Loève decomposition and a non-Gaussian stochastic model. Liu et al. [37] proposed a method for generating multi-point seismic motions on the basis of focal mechanism and analyzed the sensibility of the generated ground motions to local site effect and epicentral distance. Considering the effects of incoherence, wave passage and differential site response, Konakli et al. [38] presented a method for simulating arrays of spatially varying ground motions and validated the correctness of the method by comparing statistical characteristics of the synthetic motions with target theoretical models. Alexander [39] used real multi-station data from SMART-1 to investigate the effect of structural mode coupling. Moreover, the structural dynamic responses of transmission tower-lines [40], large embankment dams [41], bridge structures [42–47] and long tunnels [48,49] were investigated by different researchers under multi-support seismic excitations, respectively.

As mentioned above, for the seismic analysis of long-span structures, although multi-support seismic motions have been extensively studied, it has primarily focused on ground motions. Therefore, one method that can input the multi-support seismic excitations at the base of the building is urgently needed to accurately evaluate the seismic response of structures considering soil-structure interaction. This paper conducts the theoretical and numerical study for simulating the multi-support seismic underground excitations in saturated soil with overlying water for obliquely incident *SV*-waves. *SH*-wave vibrates perpendicular to its propagation and is out of plane, the behavior of *SH*-wave vibrating in saturated double-phase media, as it is known, is the same as that in single-phase medium (only including soil) based on wave theory. While, the wave equations of *SH* wave is relatively simple to solve because that it is not needed to satisfy the vertical boundaries. More over, there exist waveform transformation between the *SV*-wave and new generated *P*-wave at the media interface, which causes double-coupling wave equations. So, these equations will induce more complexity in solving the mathematical equations. Moreover, P-wave has its unique character that it can propagate in fluid media such as water. At the interface between ground and overlying water, the *SV* wave-induced new *P*-wave will propagate in the overlying water, which enhances the strength of reflected wave and affects the wave filed.

This paper proposed a approach including the specific reflection coefficients, transfer functions and the underground PSD for simulating spatially variable seismic underground motion simulation in a layering soil model with overlying water for SV wave incidence. Besides, parameter sensitivity of the predicted seismic motions to the soil thickness, incident angle and overlying water depth is investigated. In Section 2, the wave equations of saturated soil, elastic-solid media and ideal fluid are reviewed. In Section 3, the reflection coefficients at the interface between saturated soil and overlying water are derived and the transfer functions of soil layer with arbitrary depths are proposed. In Section 4, the key elements (e.g., the underground power spectral density (PSD), response spectrum function and underground coherency function) for generating the multi-support seismic underground motions and verifying the reasonability, are derived based on the transfer functions. The method of generating multi-support seismic underground motions is validated and some numerical examples are given in Section 5. In Section 6, the concluding remarks are presented.

2. Wave equations

As shown in Fig. 1, the two-dimensional system of the investigated geometric geological structure contains multi-layer saturated soil and the overlying water, which extends to infinity in the horizontal dimension and has a half-space as the bottom layer.

2.1. The wave equations in layered, saturated soil

According to the Biot porous medium theory [1–3], the motion equations in saturated soil can be expressed as follows

$$N\nabla^2 u + \nabla[(A+N)\nabla\cdot u + Q\nabla\cdot U] = \frac{\partial^2}{\partial t^2}(\rho_{11}u + \rho_{12}U) + \eta\frac{\partial}{\partial t}(u-U) \tag{1}$$

where u and U refer to the displacements of solid and fluid, respectively; η is the decay function which is denoted as $\eta = v\varphi^2/k_0$, and v is fluid viscosity coefficient. The dynamic mass coefficients are given by $\rho_{11} = (1-\varphi)\rho_s + \varphi(\alpha-1)\rho_f$, $\rho_{12} = -\varphi(\alpha-1)\rho_f$, $\rho_{22} = \varphi\alpha\rho_f$, where $\alpha = 1 + \gamma(1+\varphi)/\varphi$ with γ is the coefficient of induced inertia on solid (due to the oscillation of solid frame in fluid); ρ_f and ρ_s denote the

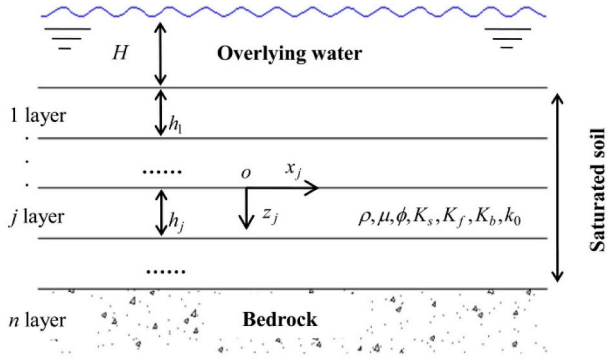

Notes: $\rho,\mu,\phi,K_s,K_f,K_b,k_o$ denote soil density, shear modulus, porosity, bulk modulus of the solid, bulk modulus of the fluid, bulk modulus of the solid skeleton and permeability coefficient of (j)th layer, respectively.

Fig. 1. Schematic diagram of site on elastic half-space.

$$\nabla[Q\nabla\cdot u + R\nabla\cdot U] = \frac{\partial^2}{\partial t^2}(\rho_{12}u + \rho_{22}U) - \eta\frac{\partial}{\partial t}(u - U) \tag{2}$$

intrinsic fluid and solid density, respectively. A, N, Q and R represent the generalized elastic parameters and satisfy the following relationships

$$A = \frac{\varphi K_b + (1-\varphi)K_f(1-\varphi-K_b/K_s)}{\varphi + K_f/K_s(1-\varphi-K_b/K_s)} - \frac{2}{3}\mu \tag{3a}$$

$$N = \mu \tag{3b}$$

$$Q = \frac{\varphi K_f(1-\varphi-K_b/K_s)}{\varphi + K_f/K_s(1-\varphi-K_b/K_s)} \tag{3c}$$

$$R = \frac{\varphi^2 K_f}{\varphi + K_f/K_s(1-\varphi-K_b/K_s)} \tag{3d}$$

where ρ, μ, φ, K_s, K_f, K_b, k_o denote the soil density, shear modulus, porosity, bulk modulus of the solid, bulk modulus of the fluid, bulk modulus of the solid skeleton and permeability coefficient of the (j)th layer, respectively.

According to the principle of Helmholtz vector decomposition, solid-fluid displacement vectors can be expressed as

$$u = \nabla\phi + \nabla\times K,\quad U = \nabla\vartheta + \nabla\times G \tag{4}$$

where ϕ and ϑ are P-wave potentials for solid and fluid, respectively; K and G are SV-wave potentials for solid and fluid, respectively. Substituting Eq. (4) into Eqs. (1) and (2), the expression forms of the four parameters can be expressed as

$$\phi = \bar{\phi}_1 + \bar{\phi}_2,\quad \vartheta = \beta_1\bar{\phi}_1 + \beta_2\bar{\phi}_2,\quad G = \alpha_0 K \tag{5}$$

$$(\nabla^2 + \delta_j^2)\bar{\phi}_j = 0,\quad (\nabla^2 + \delta_3^2)\bar{K} = 0,\quad (j = 1,2) \tag{6}$$

For the purpose of simplification, the following expressions [47] can be defined as

$$P = A + 2N,\quad M = P + R + 2Q,\quad \rho = \rho_{11} + 2\rho_{12} + \rho_{22} \tag{7a}$$

$$\sigma_{11} = P/M,\quad \sigma_{12} = Q/M,\quad \sigma_{22} = R/M,\quad \gamma_{11} = \rho_{11}/\rho,\quad \gamma_{12} = \rho_{12}/\rho,\quad \gamma_{22} = \rho_{22}/\rho \tag{7b}$$

$$E = \sigma_{11}\sigma_{22} - \sigma_{12}^2,\quad F = \gamma_{11}\sigma_{22} + \gamma_{22}\sigma_{11} - 2\gamma_{12}\sigma_{12},\quad G = \gamma_{11}\gamma_{22} - \gamma_{12}^2 \tag{7c}$$

$$b = \sigma_{12} + \sigma_{22},\quad g = \gamma_{11}\sigma_{22} - \gamma_{12}\sigma_{12},\quad h = \gamma_{22}\sigma_{12} - \gamma_{12}\sigma_{22},\quad f = \eta/\rho\omega \tag{7d}$$

$$\delta_0^2 = \rho\omega^2/M,\quad \Delta^2 = F^2 - 4EG - 2if(F - 2E) - f^2 \tag{7e}$$

$$\Omega_{1,2} = (F - if \mp \Delta)/2E,\quad \Omega_3 = (M/N)(G - if)/(\gamma_{22} - if) \tag{7f}$$

$$\delta_j^2 = \delta_0^2\Omega_j,\quad \beta_{1,2} = (g - ibf - E\Omega_{1,2})/h - ibf,\quad \alpha_0 = (\gamma_{12} + if)/(\gamma_{22} - if) \tag{7g}$$

As can be seen from Eq. (6), two kinds of compression waves and one shear wave are contained in the porous saturated medium. The phase velocities of these waves can be expressed as

$$c_k = (M/\rho)^{1/2}/\mathrm{Re}(\Omega_k^{1/2}),\quad (k = 1,2,3) \tag{8}$$

where k = 1, 2, 3 denoting $P1$, $P2$ and SV waves, respectively.

For three different waves, the following solution to Eq. (6) can be obtained [4].

$$\phi_k = E_{Pk}\exp(i\omega t - i\delta_k(xw_{k1} - zw_{k3})) + F_{Pk}\exp(i\omega t - i\delta_3(xw_{31} + zw_{33})),\quad (k = 1,2) \tag{9a}$$

$$\psi_1 = E_S\exp(i\omega t - i\delta_3(xw_{31} - zw_{k3})) + F_S\exp(i\omega t - i\delta_3(xw_{31} + zw_{33})) \tag{9b}$$

where φ_1, φ_2 and ψ_1 are the potential functions of $P1$, $P2$ and SV waves, respectively; E_{P1}, E_{P2} and E_S are the potential amplitudes of corresponding up-going waves, respectively; F_{P1}, F_{P2} and F_S are the potential amplitudes of corresponding down-going waves, respectively; w_{k1} and w_{k3} denote the component of unit vector in x-direction and z-direction. According to the Snell's law, the horizontal wave numbers (k_1) of harmonic wave are the same in x-direction

$$k_1 = \delta_k w_{k1} = \sin\theta\cdot\omega/c_k,\quad w_{k1} = (\omega/c_k\cdot\sin\theta)/\delta_k,\quad w_{k3} = (1 - w_{k1}^2)^{1/2},\quad (k = 1,2,3) \tag{10}$$

Considering the two-dimensional wave motion in both x and z directions, the displacements of solid-fluid can be expressed by the potential functions as

$$u_1 = \frac{\partial\phi_1}{\partial x} + \frac{\partial\phi_2}{\partial x} + \frac{\partial\psi_1}{\partial z},\quad u_3 = \frac{\partial\phi_1}{\partial z} + \frac{\partial\phi_2}{\partial z} - \frac{\partial\psi_1}{\partial x} \tag{11a}$$

$$U_1 = \beta_1\frac{\partial\phi_1}{\partial x} + \beta_2\frac{\partial\phi_2}{\partial x} + \alpha_0\frac{\partial\psi_1}{\partial z},\quad U_3 = \beta_1\frac{\partial\phi_1}{\partial z} + \beta_2\frac{\partial\phi_2}{\partial z} - \alpha_0\frac{\partial\psi_1}{\partial x} \tag{11b}$$

where u_1 and U_1 are the displacements along the x-direction for solid and fluid, respectively; u_3 and U_3 are the displacements along the z-direction for solid and fluid, respectively.

The stresses of solid-fluid [4] can be expressed as:

$$\sigma_{ij} = (Ae + Q\xi)\delta_{ij} + 2Ne_{ij},\quad \tau = -\varphi p = Qe + R\xi,\quad e_{ij} = \frac{1}{2}(u_{i,j} + u_{j,i})\quad (i,j = 1,3) \tag{12}$$

where δ_{ij} is Kronecker coefficient; $e = \nabla\cdot u$; $\xi = \nabla\cdot U$; p is pore pressure.

2.2. The wave equations in elastic-solid medium

Regardless of the physical force, the wave equation of the elastic solid medium can be expressed as

$$(\lambda_n + 2\mu_n)\nabla(\nabla\cdot u) - u\nabla\times(\nabla\times u_n) = \rho_n\frac{\partial^2 u_n}{\partial t^2} \tag{13}$$

where λ_n and μ_n are the Lamé's first parameter and second parameter, respectively; ρ_n is the density of elastic-solid medium.

Similar to saturated soil, the potential functions of P and SV waves can be obtained [52].

$$\phi_n = E_{Pn}\exp(i(\omega t - k_1 x + k_{3pn}z)) + F_{Pn}\exp(i(\omega t - k_1 x - k_{3pn}z)) \tag{14a}$$

$$\psi_n = E_{Sn}\exp(i(\omega t - k_1 x + k_{3Sn}z)) + F_{Sn}\exp(i(\omega t - k_1 x - k_{3Sn}z)) \tag{14b}$$

When the incident wave is SV wave, the wave numbers in different directions can be expressed as [52].

$$k_1 = \omega/c_{Sn}\cdot\sin\theta,\quad k_{3Sn} = \omega/c_{Sn}\cdot\cos\theta \tag{15a}$$

$$k_{3Pn} = \sqrt{\omega^2/c_{Pn}^2 - \omega^2/c_{Sn}^2\cdot\sin^2\theta},\quad (\sin\theta \le c_{Sn}/c_{Pn}) \tag{15b}$$

$$k_{3Pn} = -\sqrt{\omega^2/c_{Sn}^2\cdot\sin^2\theta - \omega^2/c_{Pn}^2},\quad (\sin\theta > c_{Sn}/c_{Pn}) \tag{15c}$$

where k_1 and k_{3Pn} are horizontal wave number and vertical wave number, respectively.

Considering the two-dimensional wave motion in x and z directions, the displacements and stresses can be written as

$$u_{1n} = \frac{\partial\phi_n}{\partial x} + \frac{\partial\psi_n}{\partial z},\quad u_{3n} = \frac{\partial\phi_n}{\partial z} - \frac{\partial\psi_n}{\partial x} \tag{16}$$

$$\sigma_{33n} = (\lambda + 2\mu)\phi_{n,xx} - 2\mu(\psi_{n,xz} + \phi_{n,xx}),\quad \sigma_{13n} = \mu(2\phi_{n,xz} - \psi_{n,xx} + \psi_{n,zz}) \tag{17}$$

where u_{1n} and u_{3n} are the displacements along the x-direction and z-direction, respectively; σ_{33n} and σ_{13n} are normal stress and shear stress, respectively.

2.3. The wave equations in ideal fluid

Since ideal fluid cannot bear the shearing force, i.e., the shear modulus is zero in Eq. (13), the wave equation of ideal fluid can be obtained under the disturbance condition.

$$K\nabla\nabla\cdot U_f = \rho_f\frac{\partial^2 U_f}{\partial t^2} \tag{18}$$

where K, U_f and ρ_f are the bulk modulus, the displacement and the density of ideal fluid, respectively.

The potential function of ideal fluid can be expressed as

$$\phi_f = E_{pf}\exp(i(\omega t - k_x x - k_{fz} z)) + F_{pf}\exp(i(\omega t - k_x x + k_{fz} z)) \tag{19}$$

where the wave numbers of P wave in ideal fluid are $k_f = \omega/v_f$ and $k_{fz} = \sqrt{k_f^2 - k_x^2}$; $v_f = \sqrt{K/\rho_f}$; $k_x = k_1$.

Considering the two-dimensional wave motion in both x and z directions, the displacements and pressure of fluid can be expressed as

$$U_{3f} = \frac{\partial\phi_f}{\partial z},\quad U_{1f} = \frac{\partial\phi_f}{\partial x},\quad p = -\rho_f\frac{\partial^2\phi_f}{\partial t^2} \tag{20}$$

where U_{1f} and U_{3f} are the displacements along the x-direction and z-direction, respectively; p is fluid pressure.

3. Detailed derivation process for establishing transfer function of saturated soil with overlying water layer

3.1. The refraction angles at the interface of elastic solid-saturated soil

For the plane-strain problems, three kinds of waves (i.e., $P1$, $P2$ and SV waves) are generated in the porous saturated medium when the plane SV wave incident obliquely from the bedrock to the interface of the elastic solid-saturated soil, as shown in Fig. 2.

According to the Snell's law, the horizontal wave numbers of harmonic wave are the same in x-direction. When the SV wave induced from the bedrock, we have

$$k_S\sin\theta = k_P\sin\alpha = \delta_1 w_{11} = \delta_2 w_{21} = \delta_3 w_{31} \tag{21}$$

$$k_S\sin\theta = k_P\sin\alpha = \frac{\omega}{c_1}\sin\beta_1 = \frac{\omega}{c_2}\sin\beta_2 = \frac{\omega}{c_3}\sin\beta_3 \tag{22}$$

where θ are the incident angle and reflection angle of SV wave; α is the reflection angle of P wave, respectively; β_1, β_2 and β_3 are the refraction angles of $P1$, SV and $P2$ waves, respectively.

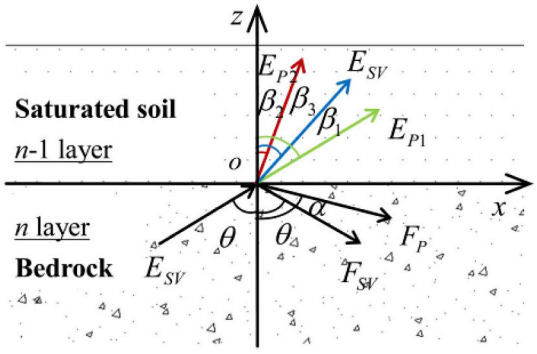

Fig. 2. Refraction and reflection at the interface of the elastic solid-saturated soil.

3.2. Derivation process of transfer matrix between bedrock and saturated soil

Based on the above analysis, each saturated soil layer has three up-going waves and three down-going waves. The amplitude vector H_j and stress-displacement vector S_j of the (j)th layer saturated soil can be expressed as

$$H_j = (E_{P1j}, F_{P1j}, E_{P2j}, F_{P2j}, E_{Sj}, F_{Sj})^T,\ (j = 1,2,3,\ldots,n-1) \tag{23}$$

$$S_j = (u_{zj}, u_{xj}, \sigma_{33j} + \tau_j, \sigma_{13j}, p_j, \varphi_j(U_{zj} - u_{zj}))^T,\ (j = 1,2,3,\ldots,n-1) \tag{24}$$

Eqs. (23) and (24) can be connected by using the following equation.

$$S_j = T_{Sj}H_j \tag{25}$$

where T_{Sj} denotes a matrix of 6 × 6, each parameter of T_{Sj} is defined in Appendix A.

In the ($j+1$)th layer, we have

$$S_{j+1} = T_{Sj+1}H_{j+1} \tag{26}$$

The continuity of stress-displacement must be satisfied between adjacent layers of saturated soil, i.e., the stress-displacement between (j)th layer and ($j+1$)th layer satisfies the following relationship.

$$S_j|_{z=h_j} = S_{j+1}|_{z=0} \tag{27}$$

Substituting Eqs. (25) and (26) into Eq. (27) yields

$$T_{Sj+1}|_{z=0}H_{j+1} = T_{Sj}|_{z=h_j}H_j \tag{28}$$

Using left multiplication inverse matrix of $T_{Sj+1}|_{z=0}$ by the two sides of Eq. (28), it arrives

$$H_{j+1} = T_{(j+1)j}H_j = T_{S(j+1)}|_{z=0}^{-1}\cdot T_{Sj}|_{z=h_j}\cdot H_j \tag{29a}$$

$$T_{(j+1)j} = T_{S(j+1)}|_{z=0}^{-1}\cdot T_{Sj}|_{z=h_j} \tag{29b}$$

where $T_{(j+1)j}$ is a matrix of 6 × 6 and denotes the transfer matrix between adjacent layer amplitude vectors.

Therefore, the amplitude vector of any layer can be associated with the first layer in accordance with the recursive Eq. (29) and expressed as

$$H_j = T_{j1}H_1 = T_{j-1}\cdot T_{j-1}\cdots T_1 H_1 \tag{30}$$

where T_{j1} is a matrix of 6 × 6.

There are two kinds of waves in bedrock, i.e., the compression wave and the shear wave. The amplitude vector H_n and the stress-displacement vector S_n of bedrock can be expressed as

$$H_n = (E_{Pn}, F_{Pn}, E_{Sn}, F_{Sn})^T,\quad S_n = (u_z, u_x, \sigma_{33}, \sigma_{13})^T \tag{31}$$

$$S_n = T_n H_n \tag{32}$$

where T_n is a matrix of 4 × 4, each parameter of T_n is defined in Appendix B.

At the interface of elastic solid-saturated soil, we have.

(1) The vertical displacement is continuous

$$u_3 = u_{3n} \tag{33a}$$

(2) The horizontal displacement is continuous

$$u_1 = u_{1n} \tag{33b}$$

(3) The normal stress is continuous

$$\sigma_{33} + \tau = \sigma_{33n} \tag{33c}$$

3.2.1. (4) the shear stress is continuous

$$\sigma_{13} = \sigma_{13n} \tag{33d}$$

(5) The relative displacement of solid-liquid is zero at the interface of elastic solid-saturated soil

$$u_3 = U_3 \tag{33e}$$

A relationship can be established between the amplitude vectors of bedrock and layered saturated soil based on the continuity conditions at the above interface of elastic solid-saturated soil.

$$(T_n|_{z=0})_{4\times4}(H_n)_{4\times1} = \left(T'_{s(n-1)}|_{z=h_{n-1}}\right)_{4\times6}(H_{n-1})_{6\times1} \tag{34}$$

where $T'_{s(n-1)}$ is the first four rows of the transpose matrix of $T_{s(n-1)}$ in the (n-1)th layer.

Define n-1 equal to j in Eq. (30), the relationship between the amplitude vectors of the bedrock and the top layer saturated soil can be expressed as

$$(H_n)_{4\times1} = T_{n1}H_1 = (T_n|^{-1}_{z=0})_{4\times4}\left(T'_{s(n-1)}|_{z=h_{n-1}}\right)_{4\times6}(T_{(n-1)1})_{6\times6}(H_1)_{6\times1} \tag{35}$$

3.3. Simplification of the top layer amplitude vector H_1

There are three kinds of up-going waves in saturated soil. Each up-going wave reaching the top of the first saturated soil layer will produce a waveform conversion. Therefore, three kinds of down-going waves are generated.

$$F_{P11} = r_{P1P1}E_{P11} + r_{P2P1}E_{P21} + r_{SP1}E_{S1} \tag{36a}$$

$$F_{P21} = r_{P1P2}E_{P11} + r_{P2P2}E_{P21} + r_{SP2}E_{S1} \tag{36b}$$

$$F_{S1} = r_{P1S}E_{P11} + r_{P2S}E_{P21} + r_{SS}E_{S1} \tag{36c}$$

where r is the reflection coefficient at the interface between saturated soil and overlying water; the nine subscripts (i.e., *P1P1, P1P2, P1S, P2P2, P2P1,P2S, SS, SP2 and SP1*) of reflection coefficients r of different up-going waves in saturated soil, respectively. Specifically, r_{P1P1} is the amplitude ratio of reflect wave of *P1* to incident wave of *P1* when the incident wave is *P1* wave, r_{P1P2} is the amplitude ratio of reflect wave of *P2* to incident wave of *P1* when the incident wave is *P1* wave, $r_{P_1S}$is the amplitude ratio of reflect wave of *S* to incident wave of *P1*when the incident wave is *P1* wave; r_{P2P2} is the amplitude ratio of reflect wave of *P2* to incident wave of *P2* when the incident wave is *P1* wave, r_{P2P1} is the amplitude ratio of reflect wave of *P1* to incident wave of *P2* when the incident wave is *P2* wave, $r_{P_2S}$is the amplitude ratio of reflect wave of *S* to incident wave of *P1* when the incident wave is *P1* wave; $r_{SS}$is the amplitude ratio of reflect wave of *S* to incident wave of *S* when the incident wave is *S* wave, $r_{SP2}$is the amplitude ratio of reflect wave of *P2* to incident wave of *S* when the incident wave is *S* wave, $r_{SP1}$is the amplitude ratio of reflect wave of *P1* to incident wave *S* of when the incident wave is *S* wave.

At the interface between saturated soil and overlying water, we have.

(1) The vertical displacement is continuous

$$u_3 = U_{3f} \tag{37a}$$

(2) The horizontal displacement is continuous

$$u_1 = U_{1f} \tag{37b}$$

(3) The normal stress is continuous

$$\sigma_{33} + \tau = -p \tag{37c}$$

(4) The shear stress is continuous

$$\sigma_{13} = 0 \tag{37d}$$

(5)The pressure is zero at the free surface of ideal fluid

$$\rho_f \frac{\partial^2 \phi_f}{\partial t^2} = 0 \tag{37e}$$

When the incident wave is *P*1 wave, i.e., $E_{P2} = 0$ and $E_{SV} = 0$, as shown in Fig. 3.

Substituting Eqs. (38a), (38b) and (38c) into Eqs. (37a) and (37e), the reflection coefficients r_{P1P1}, r_{P1P2} and r_{P1SV} can be obtained. It is noted that the incident angle θ_1 is an accumulated refraction angle when the P_1 wave spreads through the layered saturated soil.

When the incident wave is *P*2 wave, i.e., $E_{P1} = 0$ and $E_{SV} = 0$, as shown in Fig. 4.

According to Eqs. (9a) and (9b), the potential functions can be expressed as

$$\phi_1 = F_{p1}\exp(i(\omega t - \delta_1 w_{11}x + \delta_1 w_{13}z)) \tag{39a}$$

$$\phi_2 = E_{p2}\exp(i(\omega t - \delta_2 w_{21}x - \delta_2 w_{23}z)) + F_{p2}\exp(i(\omega t - \delta_2 w_{21}x + \delta_2 w_{23}z)) \tag{39b}$$

$$\psi_1 = F_s\exp(i(\omega t - \delta_3 w_{31}x + \delta_3 w_{33}z)) \tag{39c}$$

Substituting Eqs. (39a), (39b) and (39c) into Eqs. (37a) and (37e), the reflection coefficients r_{P2P1}, r_{P2P2} and r_{P2SV} can be obtained. It is noted that the incident angle θ_2 is an accumulated refraction angle when the P_2 wave spreads through the layered saturated soil.

When the incident wave is *SV* wave, i.e., $E_{P1} = 0$ and $E_{P2} = 0$, as shown in Fig. 5.

According to Eqs. (9a) and (9b), the potential functions can be expressed as

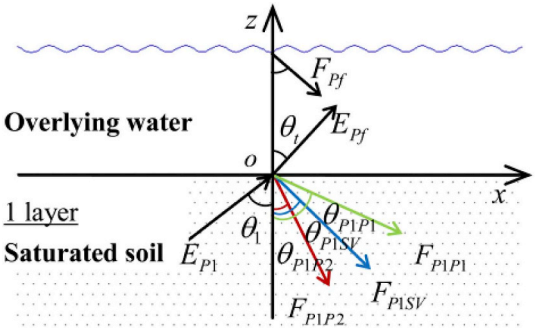

Fig. 3. The interface between saturated soil and overlying water for incident *P*1 wave. According to Eqs. (9a) and (9b), the potential functions can be expressed as.

$$\phi_1 = E_{p1}\exp(i(\omega t - \delta_1 w_{11}x - \delta_1 w_{13}z)) + F_{p1}\exp(i(\omega t - \delta_1 w_{11}x + \delta_1 w_{13}z)) \tag{38a}$$

$$\phi_2 = F_{p2}\exp(i(\omega t - \delta_2 w_{21}x + \delta_2 w_{23}z)) \tag{38b}$$

$$\psi_1 = F_s\exp(i(\omega t - \delta_3 w_{31}x + \delta_3 w_{33}z)) \tag{38c}$$

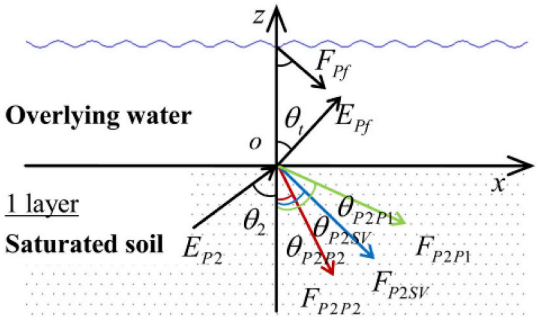

Fig. 4. The interface between saturated soil and overlying water for incident *P*2 wave.

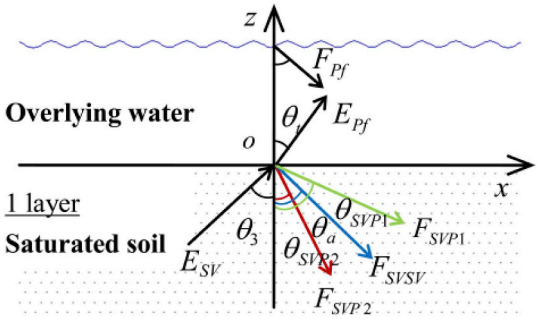

Fig. 5. The interface between saturated soil and overlying water for incident *SV* wave.

$$\phi_1 = F_{p1}\exp(i(\omega t - \delta_1 w_{11}x + \delta_1 w_{13}z)) \tag{40a}$$

$$\phi_2 = F_{p2}\exp(i(\omega t - \delta_2 w_{21}x + \delta_2 w_{23}z)) \tag{40b}$$

$$\psi_1 = E_s\exp(i(\omega t - \delta_3 w_{31}x - \delta_3 w_{33}z)) + F_s\exp(i(\omega t - \delta_3 w_{31}x + \delta_3 w_{33}z)) \tag{40c}$$

Substituting Eqs. (40a), (40b) and (40c) into Eqs. (37a) and (37e), the reflection coefficients r_{SVP1}, r_{SVP2} and r_{SVSV} can be obtained. It is noted that this incident angle θ_3 is an accumulated refraction angle when the *SV* wave spreads through the layered saturated soil.

Substituting Eqs. (36a) and (36c) into Eq. (23), the top amplitude vector H_1 can be written as

$$H_1 = (E_{P11}, r_{P1P1}E_{P11} + r_{P2P1}E_{P21} + r_{SVP1}E_{S1}, E_{P21}, r_{P1P2}E_{P11} + r_{P2P2}E_{P21} + r_{SVP2}E_{S1}, E_{S1}, r_{P1SV}E_{P11} + r_{P2SV}E_{P21} + r_{SVSV}E_{S1})^T \tag{41}$$

There are six unknowns (E_{P11}, F_{P11}, E_{P21}, F_{P21}, E_{S1}, F_{S1}) in Eq. (23) that are reduced to three unknowns (E_{P11}, E_{P21}, E_{S1}).

3.4. Establishment of transfer function

There are three unknowns (E_{P11}, E_{P21}, E_{S1}) in Eq. (41) and two unknowns (E_{Pn}, E_{Sn}) in Eq. (31). However, T_{n1} is a matrix of 4 × 6 and four equations can be established. Therefore, it is necessary to add an equation. Assuming the bedrock is impervious, i.e., $\varphi_j(U_{zj} - u_{zj}) = 0$, then a new matrix $(T_{n1})_{5\times6}$ is established and the following equations can be obtained.

$$E_{Pn} = a_{11}E_{P11} + a_{12}E_{P21} + a_{13}E_{S1} \tag{42a}$$

$$F_{Pn} = a_{21}E_{P11} + a_{22}E_{P21} + a_{23}E_{S1} \tag{42b}$$

$$E_{Sn} = a_{31}E_{P11} + a_{32}E_{P21} + a_{33}E_{S1} \tag{42c}$$

$$F_{Sn} = a_{41}E_{P11} + a_{42}E_{P21} + a_{43}E_{S1} \tag{42d}$$

$$0 = a_{51}E_{P11} + a_{52}E_{P21} + a_{53}E_{S1} \tag{42e}$$

where $a_{st}(s = 1,2,3,4,5 \quad t = 1,2,3)$ is related to H_1 and $(T_{n1})_{5\times6}$ and defined in Appendix C.

Combining Eqs. (42a) and (42c) and (42e) yields

$$E_{P11} = c_1E_{Pn} + c_2E_{Sn}, \quad E_{P21} = c_3E_{Pn} + c_4E_{Sn}, \quad E_{S1} = c_5E_{Pn} + c_6E_{Sn} \tag{43a}$$

where $c_i(i = 1,2,3,4,5,6)$ is defined in Appendix C.

When the incident wave is *SV* wave, we have $E_{Pn} = 0$. Eq. (43a) can be expressed as

$$E_{P11} = c_2E_{Sn}, \quad E_{P12} = c_4E_{Sn}, \quad E_{S1} = c_6E_{Sn} \tag{43b}$$

Substituting Eq. (43b) into Eq. (41) and the top amplitude vector H_1 can be expressed as

$$H_1 = (d_{12}E_{Sn}, d_{22}E_{Sn}, d_{32}E_{Sn}, d_{42}E_{Sn}, d_{52}E_{Sn}, d_{62}E_{Sn})^T \tag{44}$$

where

$$d_{12} = c_2, \quad d_{22} = r_{P1P1}c_2 + r_{P2P1}c_4 + r_{SVP1}c_6 \tag{45a}$$

$$d_{32} = c_4, \quad d_{42} = r_{P1P2}c_2 + r_{P2P2}c_4 + r_{SVP2}c_6 \tag{45b}$$

$$d_{52} = c_6, \quad d_{62} = r_{P1SV}c_2 + r_{P2SV}c_4 + r_{SVSV}c_6 \tag{45c}$$

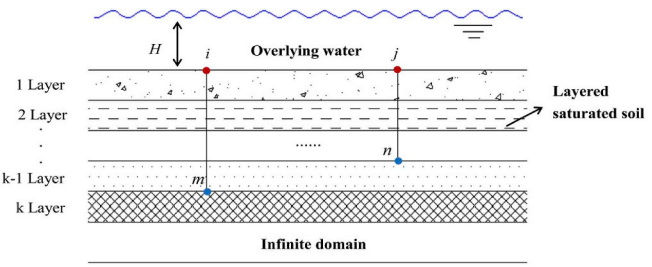

Fig. 6. Geological strata geometry containing four different points. The relationship among $S_{mm}(\omega)$, $S_{ii}(\omega)$ and $TF_{mi}(\omega)$ is.

$$\frac{S_{ii}(\omega)}{S_{mm}(\omega)} = |TF_{mi}(\omega)|^2 \tag{48}$$

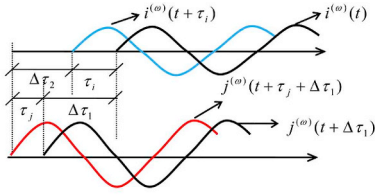

Notes: $i^{(\omega)}(t)$ and $i^{(\omega)}(t+\tau_i)$ are the harmonic motions with phase difference τ_i; $j^{(\omega)}(t+\Delta\tau_1)$ and $j^{(\omega)}(t+\Delta\tau_1+\tau_j)$ are the harmonic motions with phase difference τ_j; $\Delta\tau_1$ is the phase difference between $i^{(\omega)}(t)$ and $j^{(\omega)}(t+\Delta\tau_1)$; $\Delta\tau_2$ is the phase difference between $i^{(\omega)}(t+\Delta\tau_1)$ and $j^{(\omega)}(t+\Delta\tau_1+\tau_j)$.

Fig. 7. Harmonic motions with different phase differences.

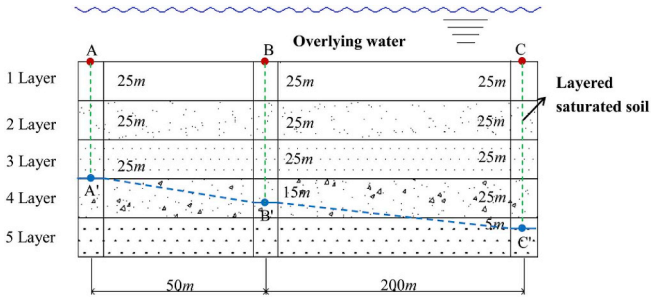

Fig. 8. Saturated soil sites with different thicknesses at different locations.

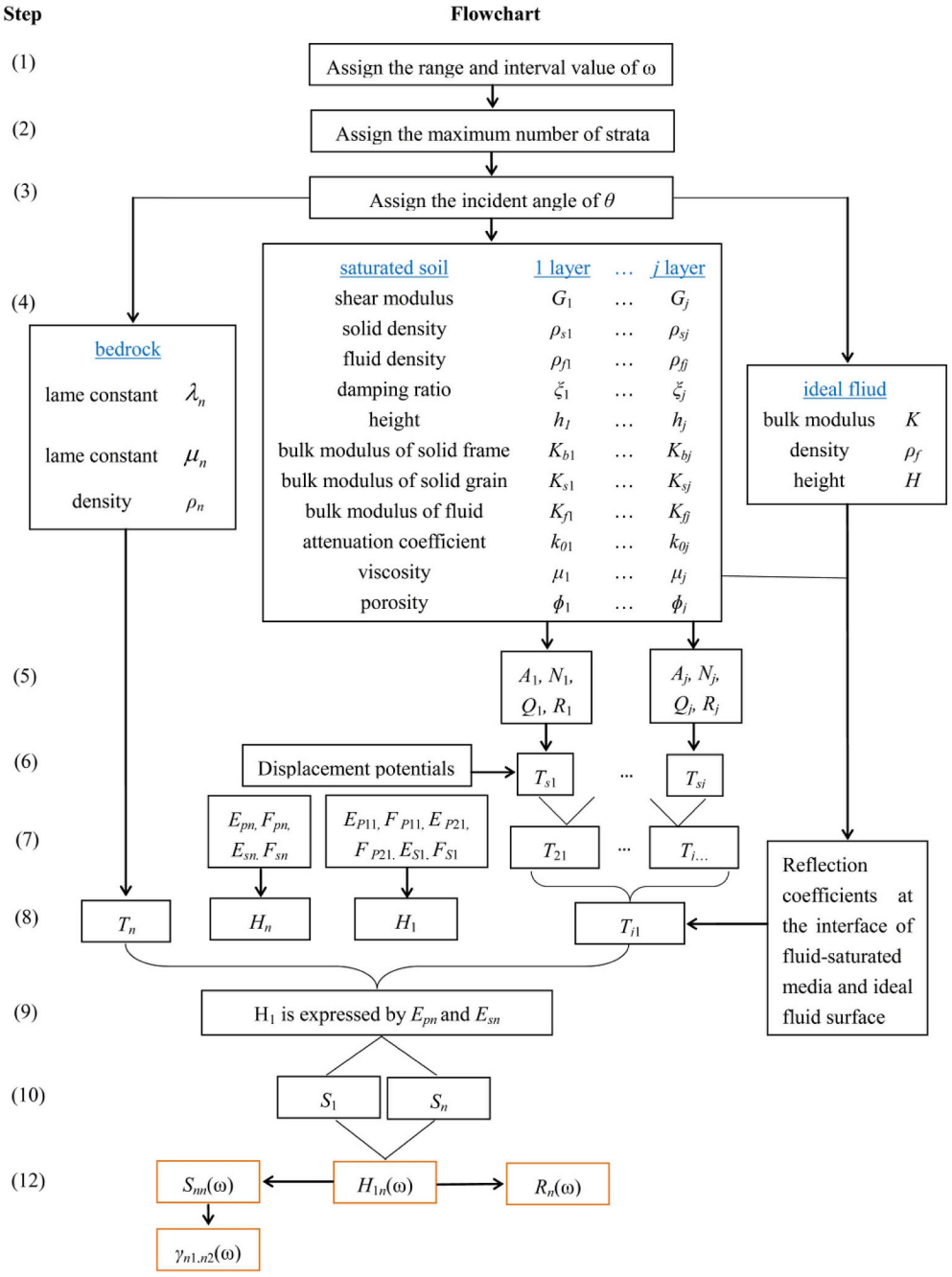

Fig. 9. Programming flowchart for calculating the PSD, response spectrum and coherence function of the underground motions in saturated soil.

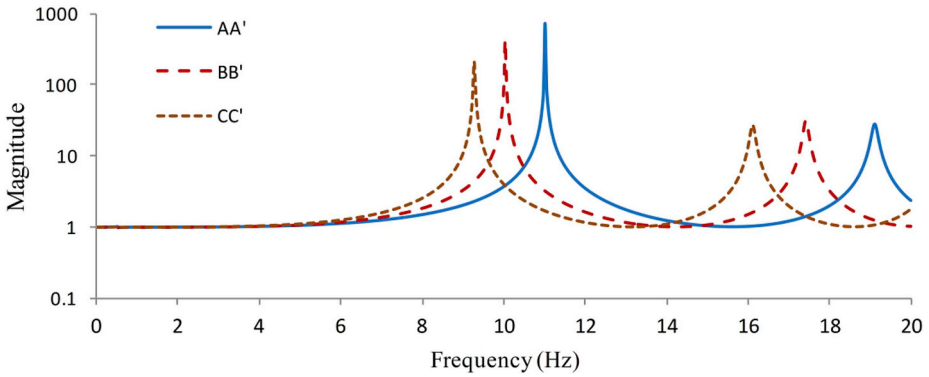

Fig. 10. Transfer functions of saturated soil at different locations.

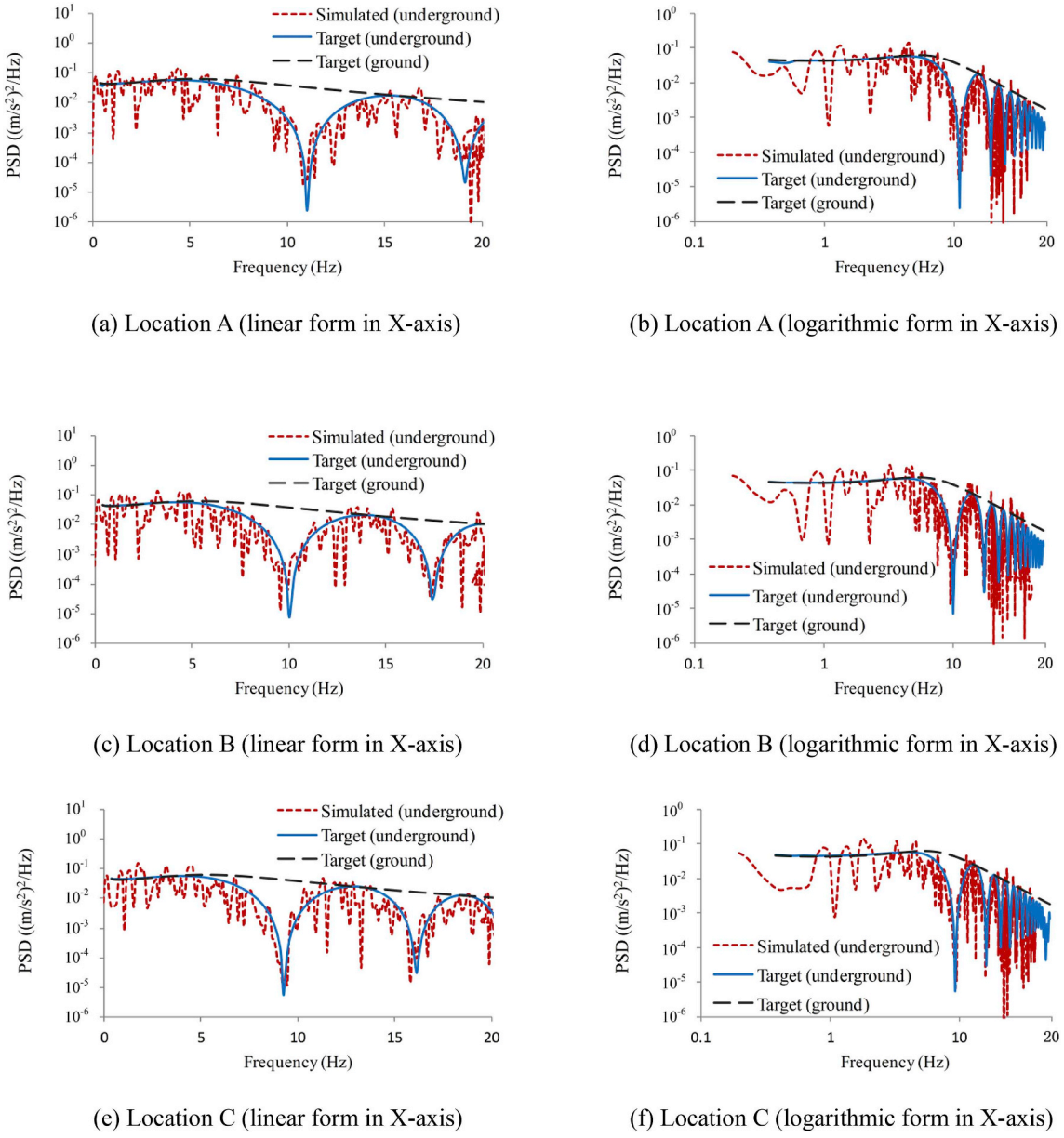

Fig. 11. Comparison between target and simulated PSD.

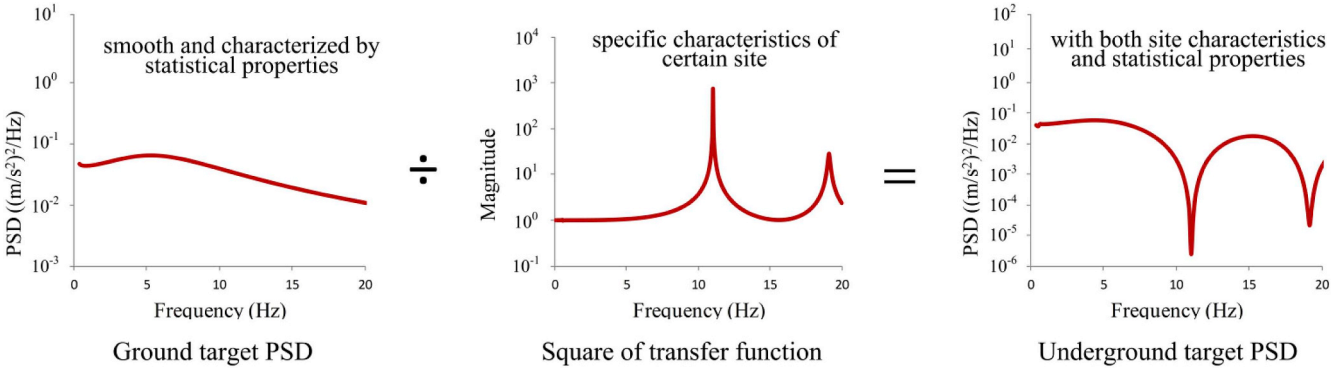

Fig. 12. The principle diagram of generating underground target PSD.

Substituting Eq. (44) into Eq. (30), the amplitude vector H_j of each soil layer is obtained, which is composition of unknowns E_{Sn}. The stress-displacement vectors of layers are obtained by taking H_j to Eq. (25).

$$S_1 = T_{S1}H_1, \quad S_j = T_{Sj}H_j = T_{j1}H_1 \tag{46}$$

The transfer function in the horizontal direction from the first layer to a lower layer can be obtained by the ratio of the second components

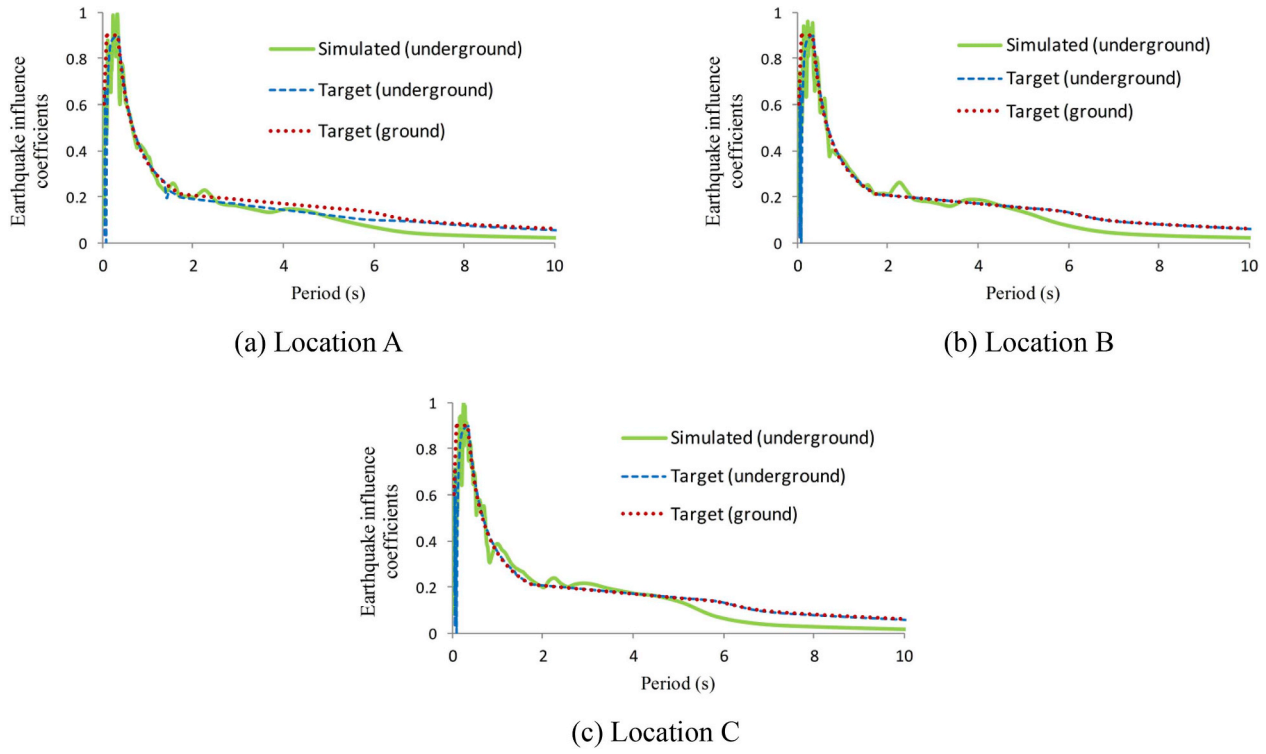

Fig. 13. Comparison between target response spectrum and simulated response spectrum.

of S_1 to S_j in the frequency domain.

$$TF_{1j}(\omega) = \frac{a_{11}}{a_{j1}} = \frac{a_{11}/\omega^2}{a_{j1}/\omega^2} = \frac{u_{11}}{u_{j1}} \tag{47}$$

where $TF_{1\ j}(\omega)$ is the transfer function between the first layer and (j)th layer and without containing E_{Sn}; a_{11} and u_{11} are the horizontal acceleration and displacement of the first layer, respectively; a_{j1} and u_{j1} are the horizontal acceleration and displacement of the (j)th layer, respectively.

4. The key elements for generating the multi-support underground motions

The underground PSD, response spectrum and the underground coherency function are three key elements for simulating the multi-support underground motions. In this section, based on the ground motion that are generated through prototype spectral representation method and the transfer functions, the underground PSD and response spectrum are first obtained and then the underground coherency function can be derived accordingly. These three theoretical models are used to establish the power spectral matrix, and the underground motions are generated by decomposing the matrix using Cholesky decomposition method.

4.1. Underground PSD and response spectrum

The geological strata geometry containing four different points is given in Fig. 6.where $S_{ii}(\omega)$ and $S_{mm}(\omega)$ are the auto-power spectrum of the motions at points i and m in saturated soils, respectively; $TF_{mi}(\omega)$ is the transfer function between (m)th layer and (i)th layer.

In this text, the Clough-Penzien model [50] is adopted as the target ground PSD (other PSD models such as Kanai-Tajimi model, Davenport model and so on can be used, too) for dynamic analysis, as shown in Fig. 11.

$$S(\omega) = \frac{\left(\omega_f^4 + 4\xi_f^2\omega_f^2\omega^2\right)\cdot S_0}{(\omega_g^2 - \omega^2) + 4\xi_g^2\omega_g^2\omega^2} \cdot \frac{\omega^4}{(\omega_f^2 - \omega^2) + 4\xi_f^2\omega_f^2\omega^2} \tag{49}$$

where S_0 is the spectral intensity; ω_g and ξ_g are the ground predominant frequency and damping ratio, respectively; ω_f and ξ_f are seismic energy parameters and $\omega^4/\left((\omega_f^2 - \omega^2) + 4\xi_f^2\omega_f^2\omega^2\right)$ represents a modified coefficient for the changes of seismic energy of low frequency. In this paper, the values of S_0, ω_g, ξ_g, ω_f and ξ_f are assigned to 0.042, 21.40, 0.075, 0.38 and 0.49, respectively [51].

Response spectrum of Bridge Seismic Design Code (MOHURD, 2011) is adopted as the target ground response spectrum, as shown in Fig. 13. The relationship between R_m (ω, ξ) and R_i (ω, ξ) in saturated soil can be expressed as

$$\frac{R_i(\omega, \xi)}{R_m(\omega, \xi)} = |TF_{mi}(\omega)| \tag{50}$$

where k is a parameter related to exceeding probability, period, circular frequency and damping ratio; R_i (ω, ξ) and R_m (ω, ξ) are the response spectra of the motions at points i and m, respectively.

4.2. Establishing underground coherency functions at different locations

As the coherence function is affected by three factors, i.e., the characteristics of site, fluid-saturated media conditions and earthquakes, the formation of ground motion will also be affected by these factors. Therefore, the structural dynamic response is uncertain. Hao coherence model [19], which describes the regional effect more accurately, is adopted as the target ground coherence function in this paper.

$$\gamma_{ij}(\omega, d) = \exp(-\beta_1 d)\cdot\exp(-a_1(\omega)\sqrt{d}\,(\omega/2\pi)^2) \tag{51}$$

where $a_1(\omega) = 2\pi/\omega + b/2\pi + c$; d is the distance between different points; β_1, a, b and c are assigned to 1.109×10^{-4}, 3.583×10^{-2}, -1.811×10^{-5} and -1.177×10^{-4} based on the 45 seismic records of SMART-1 array event [51], respectively.

Table 1
Material parameters of layered saturated soil.

Layer	Shear modulus G (MPa)	Solid density ρ_s (Kg/m^3)	Damping ratio ξ	Bulk modulus			Attenuation coefficient k_0 (m^2)	Viscosity μ (Pa × s)	Porosity ϕ
				Solid frame K_b (MPa)	Solid grain K_s (MPa)	Fluid K_f (MPa)			
1	82	2580	0.05	7610	31600	2160	1.0×10^{-10}	0.001	0.29
2	81	2600	0.05	7410	32600	2160	1.0×10^{-10}	0.001	0.30
3	80	2620	0.05	7210	33600	2160	1.0×10^{-10}	0.001	0.305
4	80	2630	0.05	7110	33800	2160	1.0×10^{-10}	0.001	0.310

The expression of the cross-PSD is given by

$$\begin{aligned} S_{ij}(\omega) &= \frac{1}{2\pi}\int_{-\infty}^{\infty} R_{ij}(\Delta\tau_1)\exp(-i\omega\Delta\tau_1)d\Delta\tau_1 \\ &= \frac{A_{(\omega)}^{\langle j\rangle}}{2\pi A_{(\omega)}^{\langle i\rangle}}\int_{-\infty}^{\infty} R_{ii}(\tau_i-\tau_j+\Delta\tau_2)\exp(-i\omega\Delta\tau_1)d\Delta\tau_1 \\ &= \frac{A_{(\omega)}^{\langle j\rangle}}{2\pi A_{(\omega)}^{\langle i\rangle}}\int_{-\infty}^{\infty} R_{ii}(\tau_i-\tau_j+\Delta\tau_2)\exp(-i\omega\Delta\tau_2)\exp(i\omega(\tau_j-\tau_i))d(\tau_i-\tau_j \\ &\quad +\Delta\tau_2) \end{aligned} \tag{52}$$

where $R_{ij}(\Delta\tau)$ is the cross-correlation function between the motions at points i and j; A represents the amplitude of harmonic vibration; τ_i and τ_j can be seen as constants here because they are determined by the given soil properties, as shown in Fig. 7; $\Delta\tau_2$ is the integral variable; superscripts i and j relate to the value of the associated variable of harmonic motions at points i and j, respectively.

It is interesting to note that the initial phase difference has no effect on the final results when the integral interval tends to infinity. Therefore, Eq. (52) can be further rewritten as

$$\begin{aligned} S_{ij}(\omega) &= \frac{A_{(\omega)}^{\langle j\rangle}}{2\pi A_{(\omega)}^{\langle i\rangle}}\int_{-\infty}^{\infty} R_{ii}(\Delta\tau_2)\exp(-i\omega\Delta\tau_2)\exp(i\omega(\tau_j-\tau_i))d\Delta\tau_2 \\ &= \frac{A_{(\omega)}^{\langle j\rangle}}{2\pi A_{(\omega)}^{\langle i\rangle}}\exp(i\omega(\tau_j-\tau_i))S_{ii}(\omega) \end{aligned} \tag{53}$$

Similarly, the cross-PSD for the underground motions, $S_{mn}(\omega)$, can be similarly expressed as

$$S_{mn}(\omega) = \frac{A_{(\omega)}^{\langle n\rangle}}{2\pi A_{(\omega)}^{\langle m\rangle}}\exp(i\omega(\tau_n-\tau_m))S_{mm}(\omega) \tag{54}$$

The two coherence functions for seismic ground and underground motions, $\gamma_{ij}(\omega)$ and $\gamma_{mn}(\omega)$, are given by

$$\gamma_{ij}(\omega) = \frac{S_{ij}(\omega)}{\sqrt{S_{ii}(\omega)S_{jj}(\omega)}},\quad \gamma_{mn}(\omega) = \frac{S_{mn}(\omega)}{\sqrt{S_{mm}(\omega)S_{nn}(\omega)}} \tag{55}$$

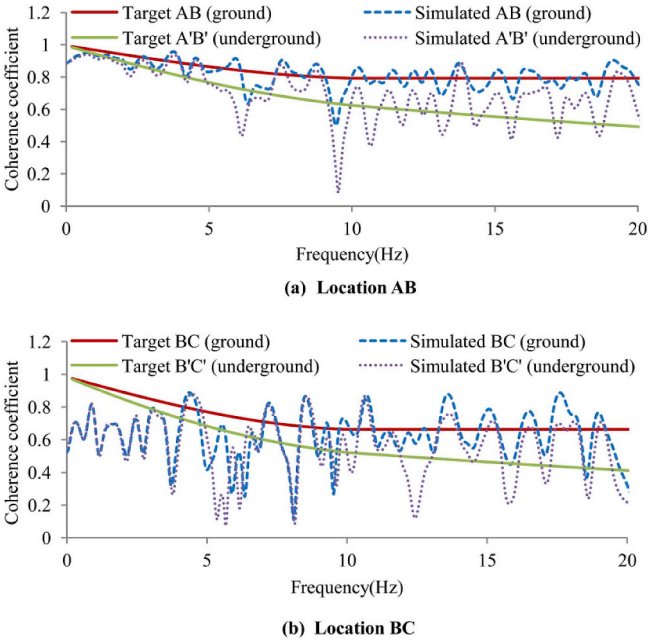

Fig. 15. Comparison between target and simulated coherence functions.

Combining Eq. (55) yields

$$\frac{\gamma_{mn}(\omega)}{\gamma_{ij}(\omega)} = \frac{S_{mn}(\omega)\cdot\sqrt{S_{ii}(\omega)S_{jj}(\omega)}}{S_{ij}(\omega)\cdot\sqrt{S_{mm}(\omega)S_{nn}(\omega)}} = \frac{S_{mn}(\omega)}{S_{ij}(\omega)}\cdot|TF_{mi}(\omega)|\cdot|TF_{nj}(\omega)| \tag{56}$$

Substituting Eqs. (53) and (54) into Eq. (56) yields

$$\begin{aligned} \frac{\gamma_{mn}(\omega)}{\gamma_{ij}(\omega)} &= \exp(i\omega(\tau_i-\tau_m))\exp(i\omega(\tau_n-\tau_j)) \\ &= \exp(i\omega((\tau_i-\tau_m)-(\tau_j-\tau_n))) \end{aligned} \tag{57}$$

The underground coherence function can be obtained based on Eqs.

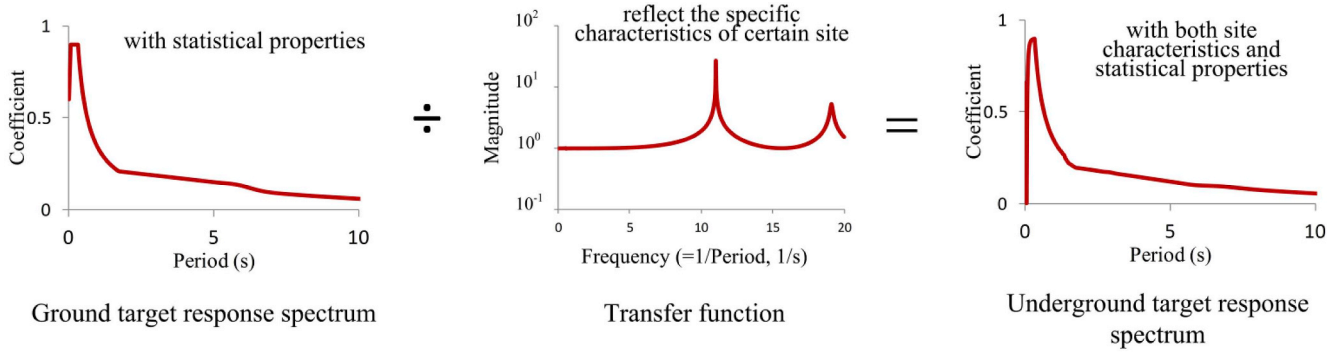

Note: The x-axis of transfer function is shown in frequency form, while the two figures of response spectrum are shown in period form.

Fig. 14. The principle diagram of generating of underground target response spectrum.

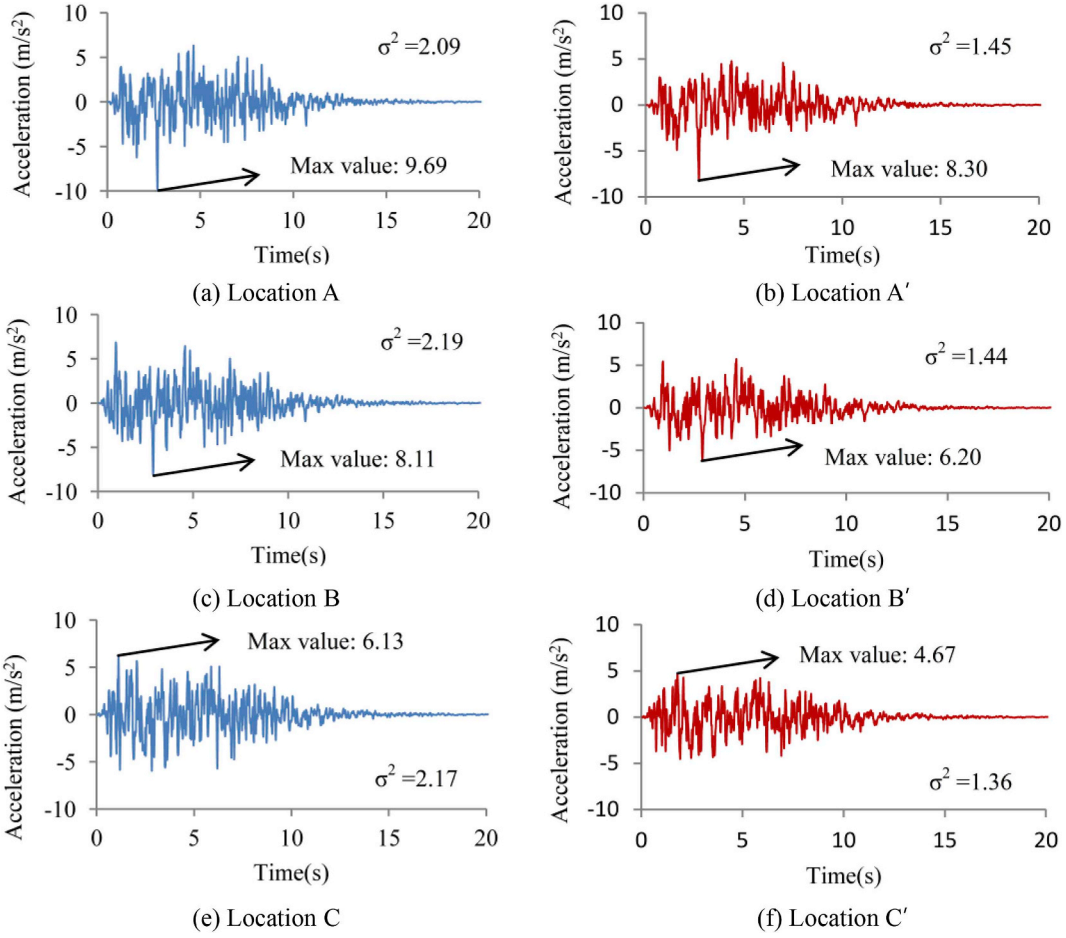

Fig. 16. Comparison between ground and underground acceleration time-histories.

(51) and (57). The values of $\tau_i\tau_j$, τ_m and τ_n can be calculated from the following equation

$$\tau = \frac{k^* z}{\omega} = \sqrt{\frac{\rho}{G^*}}z \tag{58}$$

where k^* and G^* are complex wave number and complex shear modulus and satisfy the following relationship $(k^*)^2 = \rho\omega^2/(G + i\omega\eta) = \rho\omega^2/G^*$, $G^* = G + i\omega\eta$, $\omega\eta = 2G\xi$, $G^* = G(1 + 2i\xi)$; the phase angle τ varies with the ordinate value z.

In order to obtain the appropriate multi-support seismic underground motions, the rationality of the simulated three underground necessary elements (i.e., underground power spectral density, underground response spectrum and underground coherency function) should be determined before performing an underground seismic simulation. The verification process for these three elements will be described in Section 5.1 by the numerical analysis.

According to Eq. (48), we can know that the underground motion time series have the same power spectral density function $S'(\omega)$ at every locations. Therefore, the cross power spectral density function of underground motions at n locations in a site can be written as

$$S(i\omega) = \begin{bmatrix} \gamma_{11}(\omega) & \gamma_{11}(i\omega) & \cdots & \gamma_{1n}(i\omega) \\ \gamma_{21}(i\omega) & \gamma_{22}(\omega) & \cdots & \gamma_{2n}(i\omega) \\ \cdots & \cdots & \cdots & \cdots \\ \gamma_{n1}(i\omega) & \gamma_{n2}(i\omega) & \cdots & \gamma_{nn}(i\omega) \end{bmatrix} S'(\omega) \tag{59}$$

where $\gamma_{jk}(i\omega)$ is the underground coherence function and defined in Eq. (57).Since $S(i\omega)$ is Hermitian matrix that is positive definite, it can be decomposed into the multiplication of a complex lower triangular

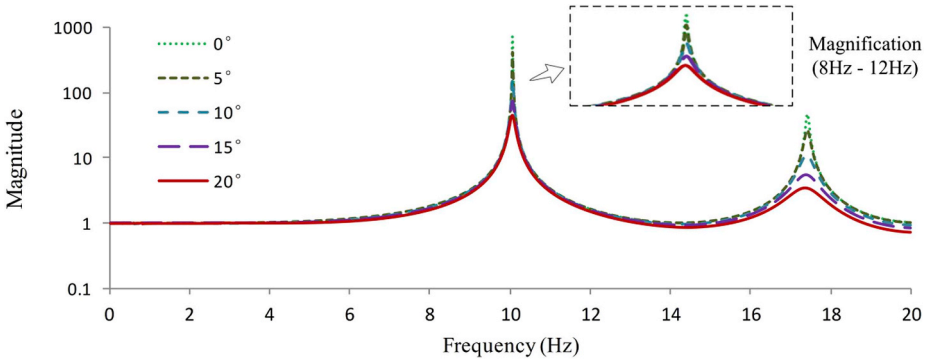

Fig. 17. Transfer functions of site soil under different incident angles (< 25°).

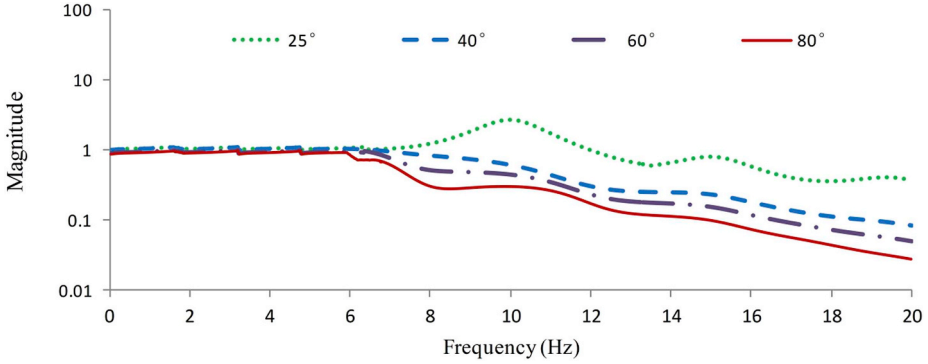

Fig. 18. Transfer functions of site soil under different incident angles (≥25°).

matrix $L(i\omega)$ and its Hermitian matrix $L^H(i\omega)$.

$$S(i\omega) = L(i\omega)L^H(i\omega)S'(\omega) \tag{60}$$

The lower triangular matrix $L(i\omega)$ can be expressed in the following form by Cholesky decomposition method [27].

$$L(i\omega) = \begin{bmatrix} L_{11}(\omega) & 0 & \cdots & 0 \\ L_{21}(i\omega) & L_{22}(\omega) & \cdots & 0 \\ \cdots & \cdots & \cdots & \cdots \\ L_{n1}(i\omega) & L_{n2}(i\omega) & \cdots & L_{nn}(i\omega) \end{bmatrix} \tag{61}$$

where

$$L_{jj}(\omega) = \left[\gamma_{jj}(\omega) - \sum_{k=1}^{j-1} L_{jk}(i\omega)L_{jk}^*(i\omega)\right]^{1/2}, \quad i = 1,2,...,n \tag{62a}$$

$$L_{jk}(i\omega) = \frac{\gamma_{jk}(i\omega) - \sum_{k=1}^{j-1} L_{jl}(i\omega)L_{kl}^*(i\omega)}{L_{kk}(\omega)} \quad k = 1,2,...,j \tag{62b}$$

After obtaining $L(i\omega)$, the stationary time series $u_j(t), j = 1, 2, \ldots, n$, can be simulated in the time domain [17].

$$u_j(t) = \sum_{m=1}^{j}\sum_{n=1}^{N} A_{jm}(\omega_n)\cos[\omega_n t + B_{jm}(\omega_n) + \phi_{mn}(\omega_n)] \tag{63}$$

where $A_{jm}(\omega) = \sqrt{4\Delta\omega}\,|L_{jm}(i\omega)|$ and $B_{jm}(\omega) = \tan^{-1}(\mathrm{Im}(L_{jm}(i\omega))/\mathrm{Re}(L_{jm}(i\omega)))$ are the amplitudes and phase angles of the simulated time histories; $\phi_{mn}(\omega_n)$ is the random phase angles uniformly distributed over the range of $[0,2\pi]$; ω_n represents an upper cut-off frequency beyond which the elements of the underground cross power spectral density matrix; $\Delta\omega$ is the resolution in the frequency domain, and $\omega_n = n\Delta\omega$ is the nth discrete frequency.

5. Numerical verification and results discussion

5.1. Verification of validity of the method

In order to verify the reliability of this method, the parameters (i.e., the PSD model, apparent wave velocity, coherency function, response spectrum, intensity envelope function, coordinates of support points and geological parameters) should be given in advance. The PSD model, response spectrum and coherency function are given in Section 4. Moreover, the apparent wave velocity is 250 m/s and the thickness of saturated soil at different locations is different as shown in Fig. 8. Based

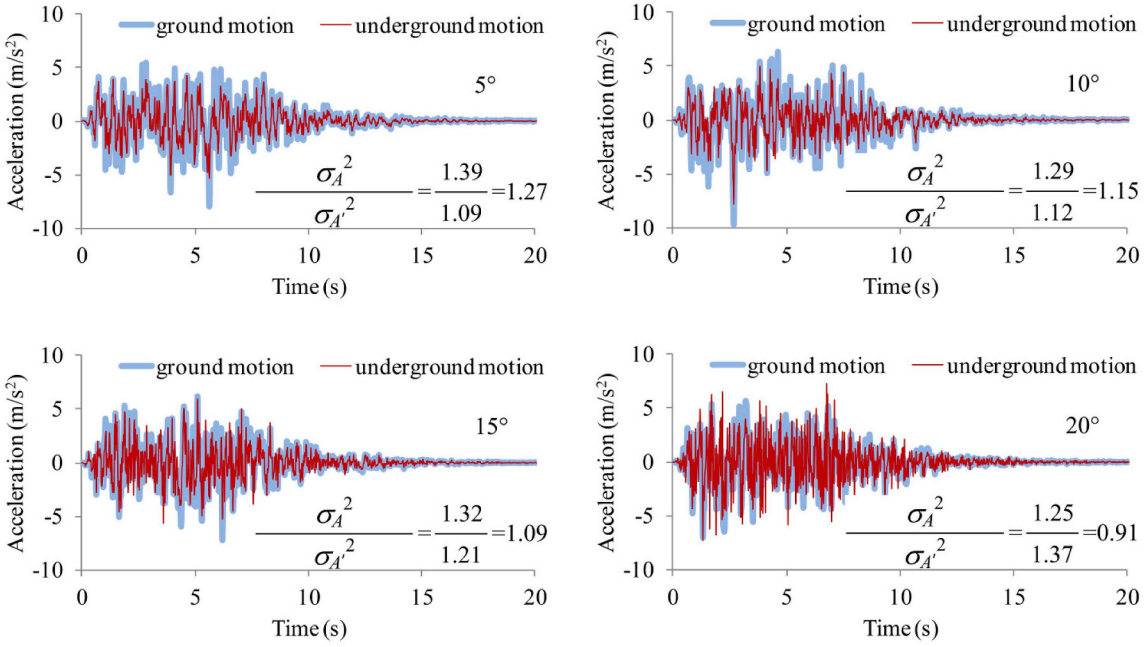

(a) point A(A′)

Fig. 19. Comparison of simulated ground and underground motions at different incident angles (5°, 10°, 15° and 20°). (a) Point A (A′); (b) point B(B′); (c) point C(C′).

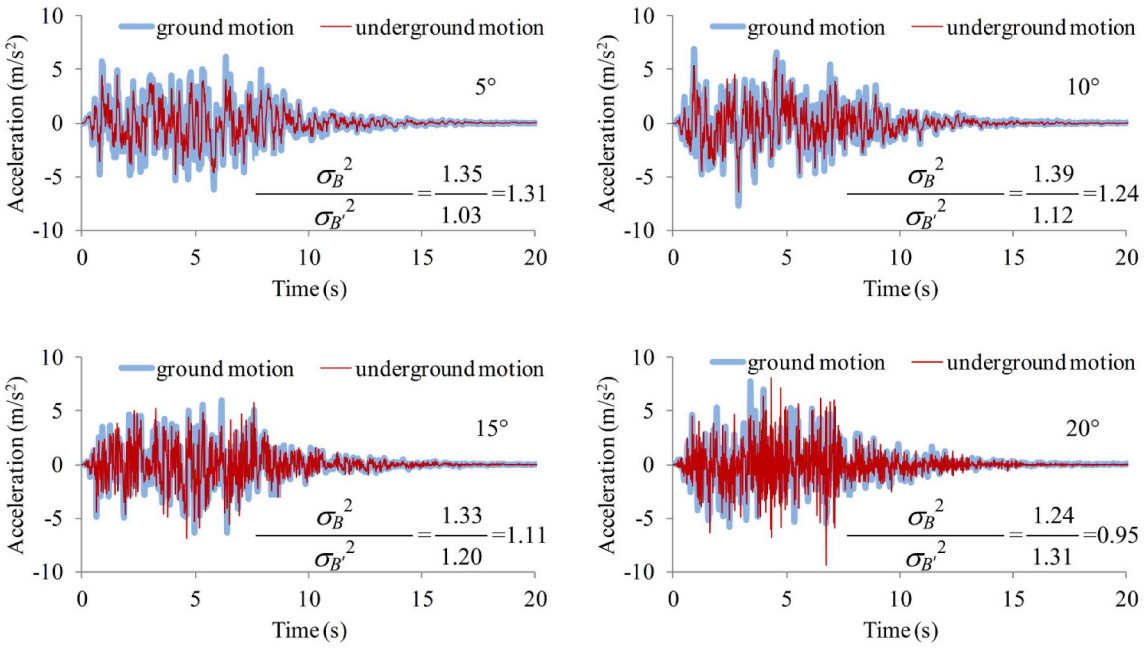

(b) point B(B′)

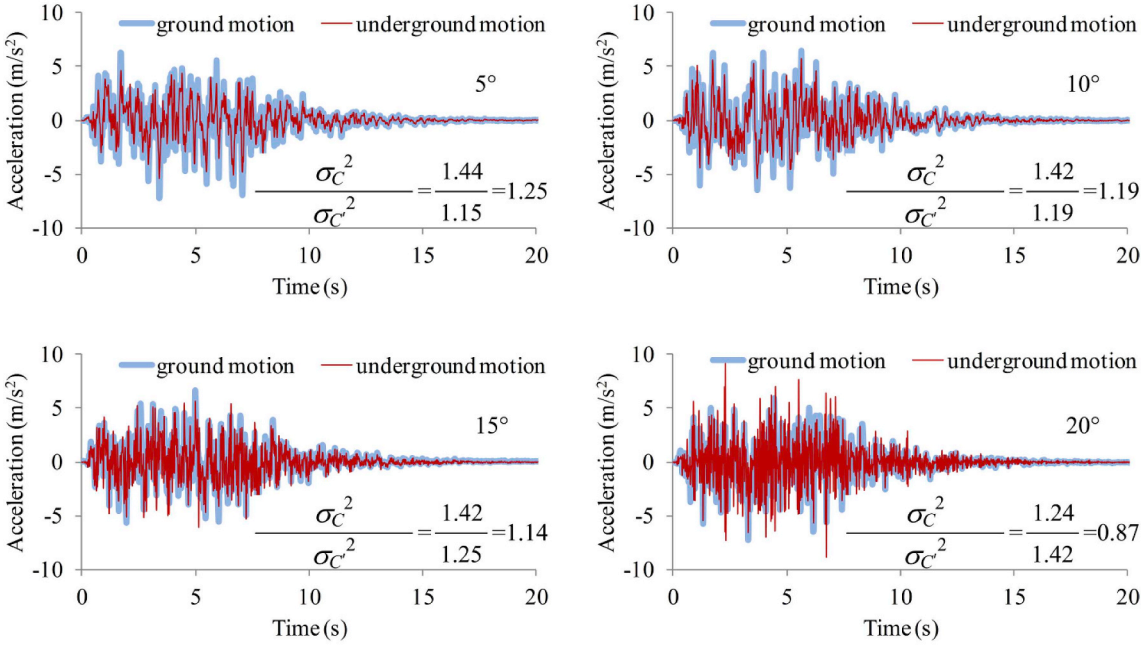

(c) point C(C′)

Fig. 19. (*continued*)

on the previous analyses, a flowchart for computing the PSD, response spectrum and coherence function of underground motions in saturated soil is shown in Fig. 9.

The parameters of saturated soil are listed in Table 1. The parameters of bedrock are defined as$\rho_n = 3000Kg/m^3$, $\mu_n = 3.0 \times 10^9\ Pa$ and$\lambda_n = 2.2 \times 10^9 Pa$. The parameters of overlying water are defined as $\rho_f = 1000Kg/m^3$ and $K = 2.16 \times 10^9 Pa$. The overlying water depth is set to be 20 m. Fig. 10 indicates that the dominant frequency of transfer function decreases with increasing thickness of saturated soils, which is consistent with the actual phenomenon and embodies the vibration characteristics of saturated soil layer. In Fig. 11, the simulated PSD of underground motions match the target PSD of underground motions in saturated soil. It should be noted that Fig. 11 uses logarithmic coordinates in the Y-axis, while uses both linear and logarithmic coordinates in the X-axis for clarity. Moreover, the underground PSD curves of saturated soil are fluctuant, which shows a great difference compared with ground PSD curves. The reason for the phenomenon is that the underground PSD is determined by the ground PSD and the transfer function which is related to the characteristics of saturated soil. Fig. 12 shows the process for the generation of underground target PSD,

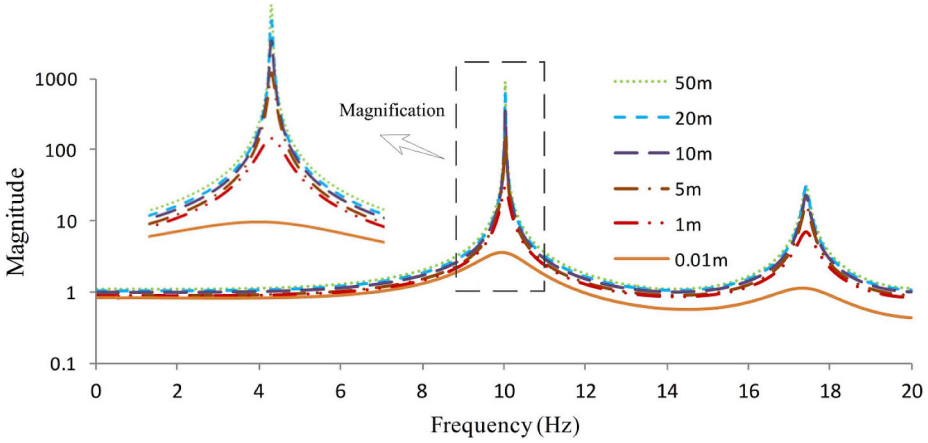

Fig. 20. Transfer functions of site soil under different overlying water depths.

which is also described in Eq. (48).

(a) Location A (linear form in X-axis) (b) Location A (logarithmic form in X-axis).

(c) Location B (linear form in X-axis) (d) Location B (logarithmic form in X-axis).

(e) Location C (linear form in X-axis) (f) Location C (logarithmic form in X-axis).

It can be seen from Fig. 13 that the underground target response spectrum curves is fluctuant while ground target response spectrum curves are smooth. Fig. 14 is drawn to explain it more clearly. The average values of underground response spectrums are smaller than the values of the platform stage of ground target response spectrums, which indicates that the seismic motions are amplified by the layered saturated soil. In addition, the simulated underground response spectrum is consistent with the target response spectrum, which demonstrates the reliability of the derived theoretical method and of the program to simulate the seismic underground motions in saturated soil with overlying water.

As shown in Fig. 15, the coherency coefficients of ground and underground are similar when the frequency is lower than 5Hz but they are significantly different when the frequency is out of range. This scenario is consistent with Eq. (58). Comparing Fig. 15 (a) with Fig. 15 (b), the coherence coefficient of BC ($B'C'$) is slightly smaller than that of AB ($A'B'$). This reflects the effect of horizontal distance on the coherence function. Moreover, the coherence coefficient of underground motions in saturated soil is smaller than that of ground motions, which reflects the effect of soil conditions on the amplification coefficient.

As we can see from Fig. 16, the peak values and variances of underground motions at different locations are smaller than those of ground motions, which is consistent with the aforementioned site amplification effect. The ratios between underground acceleration and ground acceleration decrease in order, showing that the site amplification factors of earthquake motions will become larger with increasing the thickness of saturated soil.

5.2. Effect of incident angle on simulated seismic motions and the diffrence from P-wave incidence case

In this section, the effects of the incident angle on the derived transfer function in the previous section and simulated seismic motions are investigated and the regularity is summarized. The overlying water depth is set to be 20 m and the other parameters keep unchanged. The cases for small-incident angles ($< 25^{\circ}$) and large-incident angels ($\geq 25^{\circ}$) are conducted, respectively.

Fig. 17 shows that the transfer coefficients of saturated soil under different incident angles ($< 25^{\circ}$) of points BB'. It can be seen from Fig. 17 that the peak values of transfer functions decrease with increasing incident angle. This is because there are three types of waves in the saturated soil. As the incident angle increases, a total reflection of the wave may occur in a certain layer saturated soil and the reflected wave will not be a plane wave, which will cause the energy decreasing of the up-going wave.

Fig. 18 shows that the transfer coefficients of saturated soil under different incident angles ($\geq 25^{\circ}$) of points BB'. Different from the small-angle case, the amplitude of transfer function declines steeply as the incident angle is greater than 25°. It can be seen from Fig. 18 that for a large-angle case (40°, 60° and 80°), the maximum value of the transfer function is less than 1.0, depicting that the majority of incident *SV*-wave energy exhausts during the propagation. Due to the large-incident angle, more energy consumes by the wave reflection at the layer-interface between adjacent layers.

To investigate the effect of the incident angle on the simulated seismic motions, the acceleration histories of ground and underground motions and variance ratios are given in Fig. 19. The figures show that variance ratios get smaller with the increasing incident angle. The phenomenon is consistent with that (amplitude values of transfer functions decrease with the increasing incident angle) discussed above. The total reflection components (reflection energy or downward-travelling wave energy) at the soil interface increase with increasing incidence angle, and reduces the upward-travelling wave energy (total energy conservation) and further induces the decrease of amplitude value of the transfer function. Moreover, a large incident angle may induce little ground seismic motions. The phenomenon and reasons for it are all obvious different from that under P wave incidence [[53]].

5.3. Effect of overlying water depth on simulated seismic motions

Fig. 20 shows the transfer function of the site soil under different overlying water depths (0.01 m, 1 m, 5 m, 10 m, 20 m and 50 m) of points BB'. The incident angle is set to 5°. In these cases, the overlying depths are different. Since the reflection coefficients at the interface of saturated soil and ideal fluid increases with larger overlying water depth, the amplitude of the site transfer function increases along with larger overlying water depth. However, the vibration frequency of the site mainly reflects the characteristics of the site soil. The soil parameters are identical. Therefore, the overlying water depth has no effect on the vibration frequency of the site. To further clarify the effect of overlying water depths, the acceleration histories of ground and underground motions and variance ratios are given in Fig. 21. The figures show that variance ratios get greater with the increasing overlying water depth. In essence, the phenomenon is consistent with that discussed above (i.e. amplitude values of transfer functions increase with the increasing overlying water depth).

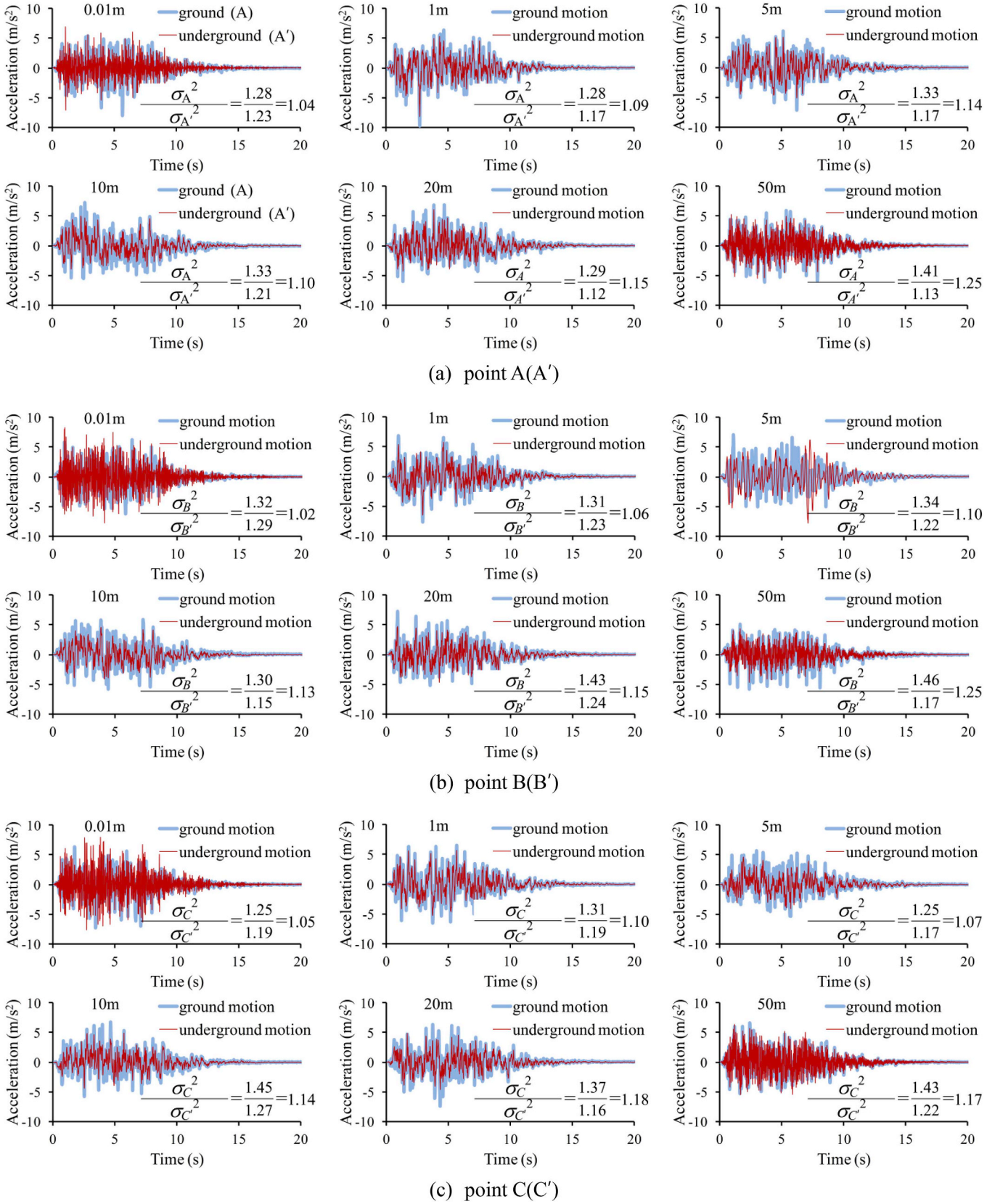

Fig. 21. Comparison of simulated ground and underground motions by different overlying water depths (0.01 m, 1 m, 5 m, 10 m, 20 m and 50 m).

6. Concluding remarks

For reasonably performing the seismic analysis of long-span structures in saturated soil with overlying water, the study of multi-support seismic underground motions considering overlying water is desirable. The main work is summarized as follows:

The reflection coefficients for obliquely incident SV waves at the interface between saturated soil and overlying water are especially

derived based on the boundary conditions. Subsequently, the transfer functions of soil layer with arbitrary depths are proposed. Three underground theoretical models (i.e., the underground PSD, response spectrum and coherency function), for establishing the underground power spectral matrix and generating multi-support seismic underground motions, are further deduced based on the presented transfer functions of saturated soil and random vibration theory. Numerical results show that the site amplification effect increases with increasing overlying water depth and decreases with increasing incident angle. Moreover, for the large-incident angle cases ($\geq 25^{\circ}$), the majority of the incident *SV*-wave energy consumes and the amplititude of transfer function declines steeply, which is obviously different from that of the small-incident angle cases and P wave incidence case [[53]].

Acknowledgements

This work was supported by the National Natural Science Foundation of China (Grant No. 51778414).

Appendix A. The parameters in T_{Sj}.

In the (j)th layer, each parameter of T_{Sj} can be expressed as

$$t_{sj11} = i\delta_1 w_{13}\exp(i\delta_1 w_{13}z),\ t_{sj12} = -i\delta_1 w_{13}\exp(-i\delta_1 w_{13}z),\ t_{sj13} = i\delta_2 w_{23}\exp(i\delta_2 w_{23}z) \tag{A.1}$$

$$t_{sj14} = -i\delta_2 w_{23}\exp(-i\delta_2 w_{23}z),\ t_{sj15} = i\delta_3 w_{33}\exp(i\delta_3 w_{33}z),\ t_{sj16} = i\delta_3 w_{33}\exp(-i\delta_3 w_{33}z) \tag{A.2}$$

$$t_{sj21} = -i\delta_1 w_{11}\exp(i\delta_1 w_{13}z),\ t_{sj22} = -i\delta_1 w_{11}\exp(-i\delta_1 w_{13}z),\ t_{sj23} = -i\delta_2 w_{21}\exp(i\delta_2 w_{23}z) \tag{A.3}$$

$$t_{sj24} = -i\delta_2 w_{21}\exp(-i\delta_2 w_{23}z),\ t_{sj25} = i\delta_3 w_{33}\exp(i\delta_3 w_{33}z),\ t_{sj26} = -i\delta_3 w_{33}\exp(-i\delta_3 w_{33}z) \tag{A.4}$$

$$t_{sj31} = -[A + (R+Q)\beta_1 + Q + 2Nw_{13}^2]\delta_1^2\exp(i\delta_1 w_{13}z) \tag{A.5}$$

$$t_{sj32} = -[A + (R+Q)\beta_1 + Q + 2Nw_{13}^2]\delta_1^2\exp(-i\delta_1 w_{13}z) \tag{A.6}$$

$$t_{sj33} = -[A + (R+Q)\beta_2 + Q + 2Nw_{23}^2]\delta_2^2\exp(i\delta_2 w_{23}z) \tag{A.7}$$

$$t_{sj34} = -[A + (R+Q)\beta_2 + Q + 2Nw_{23}^2]\delta_2^2\exp(-i\delta_2 w_{23}z) \tag{A.8}$$

$$t_{sj35} = -2N\delta_3^2 w_{31}w_{33}\exp(i\delta_3 w_{33}z),\ t_{sj36} = 2N\delta_3^2 w_{31}w_{33}\exp(-i\delta_3 w_{33}z) \tag{A.9}$$

$$t_{sj41} = 2N\delta_1^2 w_{11}w_{13}\exp(i\delta_1 w_{13}z),\ t_{sj42} = -2N\delta_1^2 w_{11}w_{13}\exp(-i\delta_1 w_{13}z) \tag{A.10}$$

$$t_{sj43} = 2N\delta_2^2 w_{21}w_{23}\exp(i\delta_2 w_{23}z),\ t_{sj44} = -2N\delta_2^2 w_{21}w_{23}\exp(-i\delta_2 w_{23}z) \tag{A.11}$$

$$t_{sj45} = -N\delta_3^2(w_{33}^2 - w_{31}^2)\exp(i\delta_3 w_{33}z),\ t_{sj46} = -N\delta_3^2(w_{33}^2 - w_{31}^2)e(-i\delta_3 w_{33}z) \tag{A.12}$$

$$t_{sj51} = (Q + R\beta_1)/\varphi\cdot\delta_1^2\exp(i\delta_1 w_{13}z),\ t_{sj52} = (Q + R\beta_1)/\varphi\cdot\delta_1^2\exp(-i\delta_1 w_{13}z) \tag{A.13}$$

$$t_{sj53} = (Q + R\beta_2)/\varphi\cdot\delta_2^2\exp(i\delta_2 w_{23}z),\ t_{sj54} = (Q + R\beta_2)/\varphi\cdot\delta_2^2\exp(-i\delta_2 w_{23}z) \tag{A.14}$$

$$t_{sj55} = 0,\ t_{sj56} = 0 \tag{A.15}$$

$$t_{sj61} = i\varphi(\beta_1 - 1)\delta_1 w_{13}\exp(i\delta_1 w_{13}z),\ t_{sj62} = -i\varphi(\beta_1 - 1)\delta_1 w_{13}\exp(-i\delta_1 w_{13}z) \tag{A.16}$$

$$t_{sj63} = i\varphi(\beta_2 - 1)\delta_2 w_{23}\exp(i\delta_2 w_{23}z),\ t_{sj64} = -i\varphi(\beta_2 - 1)\delta_2 w_{23}\exp(-i\delta_2 w_{23}z) \tag{A.17}$$

$$t_{sj65} = i\varphi(\alpha_0 - 1)\delta_3 w_{31}\exp(i\delta_3 w_{33}z),\ t_{sj66} = i\varphi(\alpha_0 - 1)\delta_3 w_{31}\exp(-i\delta_3 w_{33}z) \tag{A.18}$$

Appendix B. The parameters in T_n.

$$t_{n11} = ik_{3Pn}\exp(ik_{3Pn}z),\ t_{n12} = -ik_{3Pn}\exp(-ik_{3Pn}z) \tag{B.1}$$

$$t_{n13} = ik_1\exp(ik_{3Pn}z),\ t_{n14} = ik_1\exp(-ik_{3Pn}z) \tag{B.2}$$

$$t_{n21} = -ik_1\exp(ik_{3Pn}z),\ t_{n22} = -ik_1\exp(-ik_{3Pn}z) \tag{B.3}$$

$$t_{n23} = ik_{3Sn}\exp(ik_{3Sn}z),\ t_{n24} = -ik_{3Pn}\exp(-ik_{3Pn}z) \tag{B.4}$$

$$t_{n31} = \mu_n k_{22}\exp(ik_{3Pn}z),\ t_{n32} = \mu_n k_{22}\exp(-ik_{3Pn}z) \tag{B.5}$$

$$t_{n33} = -2\mu_n k_1 k_{3Sn}\exp(ik_{3Sn}z),\ t_{n34} = 2\mu_n k_1 k_{3Sn}\exp(-ik_{3Sn}z) \tag{B.6}$$

$$t_{n41} = 2\mu_n k_1 k_{3Pn}e^{ik_{3Pn}z},\ t_{n42} = -2\mu_n k_1 k_{3Pn}e^{-ik_{3Pn}z} \tag{B.7}$$

$$t_{n43} = \mu_n k_{33}e^{ik_{3Sn}z},\ t_{n44} = \mu_n k_{33}e^{-ik_{3Sn}z} \tag{B.8}$$

where. $k_{22} = -(k_1^2 + k_{3Pn}^2)(c_{Pn}^2/c_{Sn}^2) + 2k_1^2,\ k_{33} = k_1^2 - k_{3Sn}^2$

Appendix C. The parameters involved in Eqs. (42) and (43).

$$a_{11} = t_{n11} + t_{n12} r_{p1p1} + t_{n14} r_{p1p2} + t_{n16} r_{p1s} \tag{C.1}$$

$$a_{12} = t_{n12} r_{p2p1} + t_{n13} + t_{n14} r_{p2p2} + t_{n16} r_{p2s} \tag{C.2}$$

$$a_{13} = t_{n12} r_{sp1} + t_{n14} r_{sp2} + t_{n15} + t_{n16} r_{ss} \tag{C.3}$$

$$a_{31} = t_{n31} + t_{n32} r_{p1p1} + t_{n34} r_{p1p2} + t_{n36} r_{p1s} \tag{C.4}$$

$$a_{32} = t_{n32} r_{p2p1} + t_{n33} + t_{n34} r_{p2p2} + t_{n36} r_{p2s} \tag{C.5}$$

$$a_{33} = t_{n32} r_{sp1} + t_{n34} r_{sp2} + t_{n35} + t_{n36} r_{ss} \tag{C.6}$$

$$a_{51} = t_{n51} + t_{n52} r_{p1p1} + t_{n54} r_{p1p2} + t_{n56} r_{p1s} \tag{C.7}$$

$$a_{52} = t_{n52} r_{p2p1} + t_{n53} + t_{n54} r_{p2p2} + t_{n56} r_{p2s} \tag{C.8}$$

$$a_{53} = t_{n52} r_{sp1} + t_{n54} r_{sp2} + t_{n55} + t_{n56} r_{ss} \tag{C.9}$$

$$c_1 = \frac{-a_{53}\cdot(a_{53}\cdot a_{32} - a_{33}\cdot a_{52})}{(a_{53}\cdot a_{31} - a_{33}\cdot a_{51})\cdot(a_{53}\cdot a_{12} - a_{13}\cdot a_{52}) - (a_{53}\cdot a_{11} - a_{13}\cdot a_{51})\cdot(a_{53}\cdot a_{32} - a_{33}\cdot a_{52})} \tag{C.10}$$

$$c_2 = \frac{a_{53}\cdot(a_{53}\cdot a_{12} - a_{13}\cdot a_{52})}{(a_{53}\cdot a_{31} - a_{33}\cdot a_{51})\cdot(a_{53}\cdot a_{12} - a_{13}\cdot a_{52}) - (a_{53}\cdot a_{11} - a_{13}\cdot a_{51})\cdot(a_{53}\cdot a_{32} - a_{33}\cdot a_{52})} \tag{C.11}$$

$$c_3 = \frac{a_{53}\cdot(a_{53}\cdot a_{31} - a_{33}\cdot a_{51})}{(a_{53}\cdot a_{31} - a_{33}\cdot a_{51})\cdot(a_{53}\cdot a_{12} - a_{13}\cdot a_{52}) - (a_{53}\cdot a_{11} - a_{13}\cdot a_{51})\cdot(a_{53}\cdot a_{32} - a_{33}\cdot a_{52})} \tag{C.12}$$

$$c_4 = \frac{-a_{53}\cdot(a_{53}\cdot a_{11} - a_{13}\cdot a_{51})}{(a_{53}\cdot a_{31} - a_{33}\cdot a_{51})\cdot(a_{53}\cdot a_{12} - a_{13}\cdot a_{52}) - (a_{53}\cdot a_{11} - a_{13}\cdot a_{51})\cdot(a_{53}\cdot a_{32} - a_{33}\cdot a_{52})} \tag{C.13}$$

$$c_5 = \frac{a_{51}\cdot(a_{53}\cdot a_{32} - a_{33}\cdot a_{52}) - a_{52}\cdot(a_{53}\cdot a_{31} - a_{33}\cdot a_{51})}{(a_{53}\cdot a_{31} - a_{33}\cdot a_{51})\cdot(a_{53}\cdot a_{12} - a_{13}\cdot a_{52}) - (a_{53}\cdot a_{11} - a_{13}\cdot a_{51})\cdot(a_{53}\cdot a_{32} - a_{33}\cdot a_{52})} \tag{C.14}$$

$$c_6 = \frac{-(a_{51}\cdot(a_{53}\cdot a_{12} - a_{13}\cdot a_{52}) - a_{52}\cdot(a_{53}\cdot a_{11} - a_{13}\cdot a_{51}))}{(a_{53}\cdot a_{31} - a_{33}\cdot a_{51})\cdot(a_{53}\cdot a_{12} - a_{13}\cdot a_{52}) - (a_{53}\cdot a_{11} - a_{13}\cdot a_{51})\cdot(a_{53}\cdot a_{32} - a_{33}\cdot a_{52})} \tag{C.15}$$

where t_{nij} is a parameter of *ith* rows and *jth* columns of $(T_{n1})_{5\times6}$.

References

[1] Biot MA. Theory of propagation of elastic waves in a fluid-saturated porous solid. J Acoust Soc Am 1956;28(2):168–91.
[2] Biot MA, Willis DG. The elastic coefficients of the theory of consolidation. J Appl Mech 1957;15(2):594–601.
[3] Biot MA. Mechanics of deformation and acoustic propagation in porous media. J Appl Phys 1962;33(4):1482–98.
[4] Deresiewicz H, Rice JT. The effect of boundaries on wave propagation in a liquid-filled porous solid: III. Reflection of plane waves at a free plane boundary (general case). Bull Seismol Soc Am 1962;52(3):595–625.
[5] Deresiewicz H. The effect of boundaries on wave propagation in a liquid-filled porous solid: IV. Surface waves in a half-space. Bull Seismol Soc Am 1962;52(3):627–38.
[6] Deresiewicz H, Rice JT. The effect of boundaries on wave propagation in a liquid-filled porous solid: V. Transmission across a plane interface. Bull Seismol Soc Am 1962;54(1):409–16.
[7] Deresiewicz H. The effect of boundaries on wave propagation in a liquid-filled porous solid: VII. Surface waves in a half-space in the presence of a liquid layer. Bull Seismol Soc Am 1962;54(1):425–30.
[8] Mott G. Reflection and refraction coefficients at a fluid-solid interface. J Acoust Soc Am 1971;50(3B):819–29.
[9] Brekhovskikh LM. Waves in layered media. second ed. [M] New York: Academic Press; 1980.
[10] Dorman J. Period equation for waves of Rayleigh type on a layered, liquid-solid half space. Bull Seismol Soc Am 1962;52:389–97.
[11] Zhao CG, Gao FP, Zeng QL. The reflection and transmission of plane waves on an interface between solid and liquid-filled porous solid with dissipation of energy. Chin J Rock Mech Eng 1996;15:470–5. [in Chinese)].
[12] Petukhin A, Iwata T, Kagawa T. Study on the effect of the oceanic water layer on strong ground motion simulations. Earth Planets Space 2010;62(8):621–30.
[13] Maeda T, Furumura T, Noguchi S, Takemura S, Sakai S. Seismic- and tsunami-wave propagation of the 2011 off the pacific coast of Tohoku earthquake as inferred from the tsunami-coupled finite-difference simulation. Bull Seismol Soc Am 2013;103(2B):1456–72.
[14] Pitarka A. Modeling seawater layer effects on ground motion at ocean-bottom floor sites from offshore earthquakes. Egu General Assembly Conference 2014;16.
[15] Diao HQ, Jin J, Li L. Effect of seawater on incident plane P and SV waves at ocean bottom and engineering characteristics of offshore ground motion records off the coast of southern California, USA. Earthq Eng Eng Vib 2014;13(2):181–94.
[16] Todoriki M, Furumura T, Maeda T. Effects of sea water on elongated duration of ground motion as well as variation in its amplitude for offshore earthquakes. Geophys J Int 2017;208(1):226–33.
[17] Harichandran RS, Vanmarcke EH. Stochastic variation of earthquake ground motion in space and time. J Eng Mech 1986;112(2):154–74.
[18] Yuan X, Liao ZP. Surface motion of a cylindrical hill of circular—arc cross-section for incident plane SH waves[J]. Soil Dynam Earthq Eng 1996;15(3):189–99.
[19] Hao H. Effects of spatial variation of ground motion on large multiply-supported structures. EERC rep No 89-06, earthquake engineering research center. Berkeley: University of California; 1989.
[20] Berrah M, Kausel E. Response spectrum analysis of structures subjected to spatially varying motion. Earthq Eng Struct Dyn 1992;21(6):461–70.
[21] Lin J, Li J, Zhang W, Williams FW. Random seismic responses of multi-support structures in evolutionary inhomogeneous random fields. Earthq Eng Struct Dyn 1997;26(1):135–45.
[22] Saxena V, Deodatis G, Shinozuka M. Effect of spatial variation of earthquake ground motion on the nonlinear dynamic response of highway bridges. Proceedings, 12th world conference on earthquake engineering. 2000. Paper 2227.
[23] Zerva A, Zervas V. Spatial variation of seismic ground motions: an overview. Appl Mech Rev 2002;55(3):271–97.
[24] Zerva A. Spatial variation of seismic ground motions: modeling and engineering applications (Advances in engineering series). Boca Raton, Florida, USA: CRC Press; 2009.
[25] Wang Z, Kiureghian AD. Multiple-support response spectrum analysis using load-dependent Ritz vectors. Earthq Eng Struct Dyn 2014;43(15):2283–97.
[26] Chen B, Wang D, Li H, et al. Characteristics of earthquake ground motion on the seafloor[J]. J Earthq Eng 2015;19(6):874–904.
[27] Hao H, Oliveira CS, Penzien J. Multiple-station ground motion processing and simulation based on smart-1 array data. Nucl Eng Des 1989;111(3):293–310.
[28] Gao Y, Wu Y, Li D, et al. An improved approximation for the spectral representation method in the simulation of spatially varying ground motions[J]. Probabilist Eng Mech 2012;29:7–15.
[29] Bi KM, Hao H. Influence of irregular topography and random soil properties on coherency loss of spatial seismic ground motions. Earthq Eng Struct Dyn 2011;40(9):1045–61.
[30] Bi KM, Hao H. Modelling and simulation of spatially varying earthquake ground motions at sites with varying conditions. Probabilist Eng Mech 2012;29:92–104.

[31] Wu Y, Gao Y, Li D. Error assessment of multivariate random processes simulated by a conditional-simulation method[J]. J Eng Mech 2014;141(5). 04014155.
[32] Wu Y, Gao Y, Zhang N, et al. Simulation of spatially varying non-Gaussian and nonstationary seismic ground motions by the spectral representation method[J]. J Eng Mech 2017;144(1). 04017143.
[33] Deodatis G. Non-stationary stochastic vector processes: seismic ground motion applications. Probabilist Eng Mech 1996;11(3):149–67.
[34] Deodatis G, Arwade S, Shinozuka M. Seismic response of bridges to differential support ground motion. National Center for Earthquake Engineering Research 1997;97–0005:223–36.
[35] Cacciola P, Deodatis G. A method for generating fully non-stationary and spectrum-compatible ground motion vector processes[J]. Soil Dynam Earthq Eng 2011;31(3):351–60.
[36] Zentner I, Poirion F. Enrichment of seismic ground motion databases using Karhunen–Loève expansion. Earthq Eng Struct Dyn 2012;41(14):1945–57.
[37] Liu GH, Lu XZ, Guo W. Multi-point seismic motions based on focal mechanism and considering local site multi-layer soil effect: theory and program implementation. Chin J Comput Mech 2012;29(4):582–8. [in Chinese)].
[38] Konakli K, Kiureghian AD. Simulation of spatially varying ground motions including incoherence, wave-passage and differential site-response effects. Earthq Eng Struct Dyn 2012;41(3):495–513.
[39] Alexander NA. Multi-support excitation of single span bridges, using real seismic ground motion recorded at the SMART-1 array. Comput Struct 2008;86(1–2):88–103.
[40] Tian L. Seismic response of power transmission tower-line system under multi-component multi-support excitations. Journal of Earthquake & Tsunami 2012;6(4):389–96.
[41] Davoodi M, Jafari MK, Sadrolddini SMA. Effect of multi-support excitation on seismic response of embankment dams. Int J Civ Eng 2013;11(1B):19–28.
[42] Zhang Y, Conte JP, Yang Z, Elgamalm A, Bielak J, Acero G. Two-dimensional nonlinear earthquake response analysis of a bridge-foundation-ground system. Earthq Spectra 2008;24(2):343–86.
[43] Lou L, Zerva A. Effects of spatially variable ground motions on the seismic response of skewed, multi-span, RC highway bridge. Soil Dynam Earthq Eng 2005;25(7–10):729–40.
[44] Zhang N, Xia H, Roeck GD. Dynamic analysis of a train-bridge system under multi-support seismic excitations. J Mech Sci Technol 2010;24(11):2181–8.
[45] Guo W, Yu ZW, Guo Z. Possible existing seismic analysis errors of long span structures and bridges while utilizing multi-point earthquake calculation models. Bull Earthq Eng 2013;11(5):1683–710.
[46] Hu L, Xu YL, Zheng Y. Conditional simulation of spatially variable seismic ground motions based on evolutionary spectra. Earthq Eng Struct Dyn 2012;41(15):2125–39.
[47] Shrestha B, Hao H, Bi K. Effectiveness of using rubber bumper and restrainer on mitigating pounding and unseating damage of bridge structures subjected to spatially varying ground motions. Eng Struct 2014;79:195–210.
[48] Yuan Y, Yu HT, Li C, Yan X, Yuan JY. Multi-point shaking table test for long tunnels subjected to non-uniform seismic loadings-Part I: theory and validation. Soil Dynamics & Earthquake Engineering; 2016.
[49] Yu HT, Yuan Y, Xu GP, Su QK, Yan X, Li C. Multi-point shaking table test for long tunnels subjected to non-uniform seismic loadings-part II: application to the HZM immersed tunnel. Soil Dynamics & Earthquake Engineering; 2016.
[50] Clough RW, Penzien J. Dynamics of structures. second ed. New York: McGraw-Hill, Inc.; 1993.
[51] Kaul MK. Stochastic characterization of earthquakes through their response spectrum. Earthq Eng Struct Dyn 1978;6(5):497–509.
[52] Zhang C, Liu Q, Deng P. Surface motion of a half-space with a semicylindrical canyon under P, SV, and Rayleigh waves. Bull Seismol Soc Am 2017;107(2):809–20.
[53] Liu GH, Yu HT, Liu YQ, Lian JJ. An approach for predicting multi-support seismic underground motions in layered saturated soil under surface water. Soil Dyn Earthq Eng 2018;115:104–18.